

## PROPERTIES OF BULGELESS DISK GALAXIES II. STAR FORMATION AS A FUNCTION OF CIRCULAR VELOCITY

LINDA C. WATSON<sup>1,2</sup>, PAUL MARTINI<sup>2,3</sup>, UTE LISENFELD<sup>4</sup>, MAN-HONG WONG<sup>2,5</sup>, TORSTEN BÖKER<sup>6</sup>, EVA SCHINNERER<sup>7</sup>  
*Draft version October 13, 2018*

### ABSTRACT

We study the relation between the surface density of gas and star formation rate in twenty moderately-inclined, bulgeless disk galaxies (Sd-Sdm Hubble types) using CO(1–0) data from the IRAM 30 m telescope, H I emission line data from the VLA/EVLA, H $\alpha$  data from the MDM Observatory, and PAH emission data derived from *Spitzer* IRAC observations. We specifically investigate the efficiency of star formation as a function of circular velocity ( $v_{\text{circ}}$ ). Previous work found that the vertical dust structure and disk stability of edge-on, bulgeless disk galaxies transition from diffuse dust lanes with large scale heights and gravitationally-stable disks at  $v_{\text{circ}} < 120 \text{ km s}^{-1}$  ( $M_* \lesssim 10^{10} M_{\odot}$ ) to narrow dust lanes with small scale heights and gravitationally-unstable disks at  $v_{\text{circ}} > 120 \text{ km s}^{-1}$ . We find no transition in star formation efficiency ( $\Sigma_{\text{SFR}}/\Sigma_{\text{HI}+\text{H}_2}$ ) at  $v_{\text{circ}} = 120 \text{ km s}^{-1}$ , or at any other circular velocity probed by our sample ( $v_{\text{circ}} = 46 - 190 \text{ km s}^{-1}$ ). Contrary to previous work, we find no transition in disk stability at any circular velocity in our sample. Assuming our sample has the same dust structure transition as the edge-on sample, our results demonstrate that scale height differences in the cold interstellar medium of bulgeless disk galaxies do not significantly affect the molecular fraction or star formation efficiency. This may indicate that star formation is primarily affected by physical processes that act on smaller scales than the dust scale height, which lends support to local star formation models.

*Subject headings:* galaxies: spiral — galaxies: star formation — galaxies: ISM — radio lines: galaxies

### 1. INTRODUCTION

High resolution studies of the Milky Way and nearby galaxies show that star formation mainly occurs in giant molecular clouds (GMCs), with typical GMC masses between about  $10^3$  and  $10^7 M_{\odot}$  and radii between about ten and several hundred parsecs (e.g., Fukui & Kawamura 2010). It is challenging to study molecular gas on these scales in even the nearest galaxies ( $\lesssim 4 \text{ Mpc}$ ; e.g., Bolatto et al. 2008) and studies of more distant galaxies can only currently investigate the average properties of gas and stars on larger scales. An advantage of more distant galaxies is that they exhibit a much wider range of physical properties, which enables investigation into the influence of environment (e.g., mid-plane pressure, metallicity, and scale height) and processes that act on large scales (e.g., shear and large-scale gravitational instabilities) on star formation.

Extragalactic studies of star formation have found that the star formation rate (SFR) surface density ( $\Sigma_{\text{SFR}}$ ) and gas surface density ( $\Sigma_{\text{gas}}$ ) are correlated in the form of the Kennicutt-Schmidt law:  $\Sigma_{\text{SFR}} \propto \Sigma_{\text{gas}}^N$  (Schmidt

1959; Kennicutt 1998). This star formation law has been studied by averaging over scales as small as about 100 pc and as large as the entire optical disk. Recent high-resolution studies have found that the SFR surface density is more strongly correlated with the molecular gas surface density ( $\Sigma_{\text{H}_2}$ ) than with the atomic gas surface density ( $\Sigma_{\text{HI}}$ ), with  $\Sigma_{\text{SFR}} \propto \Sigma_{\text{H}_2}^N$  and  $N$  between 0.8 and 1.5 (Wong & Blitz 2002; Kennicutt et al. 2007; Bigiel et al. 2008; Blanc et al. 2009; Schrubba et al. 2010; Liu et al. 2011; Rahman et al. 2011). This result confirms, from an extragalactic perspective, that stars form from molecular gas and has led to an expansion in the scope of many star formation studies to investigate how environment and large-scale processes affect the molecular fraction in the interstellar medium (ISM).

Leroy et al. (2008) addressed environmental effects on the molecular fraction and star formation efficiency (SFE) with high-quality, 750 pc-resolution observations of  $\Sigma_{\text{SFR}}$ ,  $\Sigma_{\text{HI}}$ , and  $\Sigma_{\text{H}_2}$  over the optical disk of 23 nearby galaxies. They compared these observations to many star formation models and thresholds and concluded that no model fit the data sufficiently well to be declared a clear favorite. This result led them to suggest that physics that acts on scales smaller than their resolution is most important for setting the molecular fraction and SFE.

While no model was an ideal fit to the data presented in Leroy et al. (2008), the best fit was arguably with a model in which the ratio of molecular to atomic surface density is related to the mid-plane pressure ( $P_{\text{h}}$ ):  $R_{\text{mol}} \equiv \Sigma_{\text{H}_2}/\Sigma_{\text{HI}} \propto P_{\text{h}}^{\alpha}$ , and the molecular SFE (SFE[ $\text{H}_2$ ]) is constant, such that  $\text{SFE} \equiv \Sigma_{\text{SFR}}/\Sigma_{\text{HI}+\text{H}_2} = \text{SFE}(\text{H}_2) \frac{R_{\text{mol}}}{R_{\text{mol}}+1}$ . Leroy et al. (2008) noted that a model where the molecular SFE is constant requires the population of GMCs in any region to be

<sup>1</sup> Harvard-Smithsonian Center for Astrophysics, 60 Garden Street, Cambridge, MA 02138, USA; lwatson@cfa.harvard.edu

<sup>2</sup> Department of Astronomy, The Ohio State University, 140 West 18th Avenue, Columbus, OH 43210, USA

<sup>3</sup> Center for Cosmology and AstroParticle Physics, The Ohio State University, 191 West Woodruff Avenue, Columbus, OH 43210, USA

<sup>4</sup> Departamento de Física Teórica y del Cosmos, Universidad de Granada, Spain

<sup>5</sup> Department of Physics, University of Illinois, 1110 West Green Street, Urbana, IL 61801, USA

<sup>6</sup> European Space Agency, Keplerlaan 1, 2200 AG Noordwijk, The Netherlands

<sup>7</sup> Max-Planck-Institut für Astronomie, Königstuhl 17, D-69117 Heidelberg, Germany

sampled from the same distribution of properties (e.g., size and mass), independent of environment. Furthermore, once GMCs form, the general environment cannot have a strong influence on their properties. Finally, one must compare the model to observations with a number of GMCs per resolution element so as to average over evolutionary effects. Elmegreen (1993) predicted that  $R_{\text{mol}}$  should depend on the mid-plane pressure and the interstellar radiation field ( $j$ ):  $R_{\text{mol}} \propto P_{\text{h}}^{2.2} j^{-1}$ . Assuming  $\Sigma_{\text{SFR}} \propto \Sigma_{\text{H}_2}$  and  $j \propto \Sigma_{\text{SFR}}$ , the model predicts  $R_{\text{mol}} \propto P_{\text{h}}^{\alpha}$ , with  $\alpha = 1.2$ . Wong & Blitz (2002) studied seven molecular-dominated spiral galaxies and found  $\alpha = 0.8$ , while Blitz & Rosolowsky (2006) found  $\alpha = 0.92$  in their study of fourteen galaxies with a large range of  $R_{\text{mol}}$ . Values between  $\alpha = 0.5$  and 1.2 encompass most of the Leroy et al. (2008) data on the SFE versus  $P_{\text{h}}$  plane.

Ostriker et al. (2010) recently presented a star formation model that produces an approximately linear relationship between  $R_{\text{mol}}$  and  $P_{\text{h}}$ . The authors divided the ISM into a diffuse component and a gravitationally bound component. The fraction of gas in each component is set by the requirement that gas pressure in the diffuse component is balanced by the gravity of stars, dark matter, and gas (both diffuse and bound), while heating (mainly by ultraviolet (UV) photons from O and B stars formed in the bound component) balances cooling. The model assumes that the SFE within the gravitationally bound component is constant. Bolatto et al. (2011) added a metallicity-dependent heating term to the Ostriker et al. (2010) model, which resulted in agreement between the large H I surface densities observed in the Small Magellanic Cloud and the surface density of diffuse gas calculated with the adjusted Ostriker et al. (2010) model.

Another leading star formation model is that of Krumholz et al. (2009), where the molecular fraction is determined by processes that act on scales no larger than  $\sim 100$  pc, which is the size of atomic-molecular complexes in the model. Specifically, the molecular fraction is set by the balance between the formation of molecular hydrogen on the surfaces of dust grains and the destruction of molecular hydrogen by UV photons. Both dust shielding and  $\text{H}_2$  self-shielding contribute to the survival of molecular hydrogen in the interior of the complexes. Stars form only from molecular gas and the model produces a constant molecular SFE because properties of molecular clouds, like  $\Sigma_{\text{H}_2}$ , are independent of general ISM conditions, at least while gas surface densities in the general ISM are less than GMC densities ( $\sim 85 M_{\odot} \text{pc}^{-2}$ ).

In this paper, we study star formation in a sample of 20 bulgeless disk galaxies. Bulgeless galaxies are interesting from a number of perspectives. Their existence in relatively large numbers ( $\gtrsim 15\%$  of disk galaxies; Kautsch et al. 2006; Kormendy et al. 2010) provides an important constraint on hierarchical galaxy formation models, in which galaxies generally have rich merger histories that lead to bulge growth. The agreement between models and observations is becoming better as feedback, high gas fractions, and satellite mergers on radial orbits are included in the models (Robertson et al. 2006, Hopkins et al. 2008, Brook et al. 2011; but see also Scannapieco et al. 2011). Under the assumption that bulges do form when significant merger events occur,

bulgeless galaxies are a suitable sample to study secular evolution, where internal processes like star formation lead to changes in the galaxies, such as bulge growth (Kormendy & Kennicutt 2004)

A number of works have studied the components of star formation in late-type disk galaxies. Böker et al. (2003) found that their sample of 47 late-type spirals are similar to earlier-type spirals in that they fall on the approximately linear correlation between far-infrared (FIR) luminosity, which traces star formation, and the molecular hydrogen mass within the central few kpc. Furthermore, Matthews et al. (2005) found that low-surface brightness, late-type disks lie on this same relation. Dalcanton et al. (2004) studied the dust and cold ISM structure in a sample of 49 edge-on bulgeless disk galaxies. They inferred that there is a sharp transition in dust lane structure with circular velocity ( $v_{\text{circ}}$ ) based on measurements of  $R - K$  color versus height above the midplane. Galaxies with  $v_{\text{circ}} < 120 \text{ km s}^{-1}$  (we also refer to these as low- $v_{\text{circ}}$  galaxies) appear to have no dust lanes while galaxies with  $v_{\text{circ}} > 120 \text{ km s}^{-1}$  (high- $v_{\text{circ}}$  galaxies) have well-defined dust lanes (the stellar mass Tully-Fisher relation relates  $v_{\text{circ}} = 120 \text{ km s}^{-1}$  with  $M_{\star} \sim 10^{10} M_{\odot}$ ; Bell & de Jong 2001). The authors concluded that the transition is likely due to a transition in dust scale height rather than due to a sharp transition in the quantity of dust present: low- $v_{\text{circ}}$  galaxies have diffuse dust lanes with large scale heights while high- $v_{\text{circ}}$  galaxies have dust lanes with smaller scale heights. They came to this conclusion because the dust structure transition occurs over a relatively narrow range in circular velocity ( $\sim 10 \text{ km s}^{-1}$ ), and therefore over a relatively narrow range in gas and total mass, where the dust-to-gas ratio (DGR) does not vary substantially.

Dalcanton et al. (2004) also found that disk stability, parametrized by a generalized Toomre Q parameter including both gas and stars (Rafikov 2001), is correlated with the dust structure, with low- $v_{\text{circ}}$  galaxies generally stable and high- $v_{\text{circ}}$  galaxies generally unstable. Furthermore, they concluded that a sharp change in the contribution of turbulence to the stability parameter is the likely cause of the stability and dust scale height transitions. The authors suggested that high- $v_{\text{circ}}$  galaxies have turbulence dominated by supernovae explosions and gravitational instabilities while low- $v_{\text{circ}}$  galaxies have turbulence dominated by only supernovae. Independent of the source of the turbulence, the turbulent velocities must be lower in the high- $v_{\text{circ}}$  galaxies to explain the stability results. An alternative interpretation for the dust structure transition is that it is due to differences in stellar surface density and dust opacity, as suggested by Hunter & Elmegreen (2006).

Dalcanton et al. (2004) noted that the cold, star-forming gas should have a similar distribution to the dust, with larger scale heights in low- $v_{\text{circ}}$  galaxies compared to high- $v_{\text{circ}}$  galaxies. They hypothesized that a transition in SFE might accompany the transition in dust scale height and stability if the volume density of gas is the relevant quantity for setting the SFR. A low- $v_{\text{circ}}$  galaxy with a larger scale height but the same  $\Sigma_{\text{gas}}$  relative to a high- $v_{\text{circ}}$  galaxy will have a lower gas volume density ( $\rho_{\text{gas}}$ ). The low- $v_{\text{circ}}$  galaxy likely also has a lower gas pressure because pressure is proportional to the gas volume density ( $P \propto \rho_{\text{gas}} \sigma_{\text{gas}}^2$ , where  $\sigma_{\text{gas}}$  is the gas ve-

locity dispersion). In the context of the star formation model where the molecular fraction is set by the mid-plane pressure, we then expect lower  $R_{\text{mol}}$ ,  $\Sigma_{\text{SFR}}$ , and SFE in the low- $v_{\text{circ}}$  galaxy.

In this paper, we address whether there is a SFE transition at  $v_{\text{circ}} = 120 \text{ km s}^{-1}$  in our sample of bulgeless disk galaxies (Section 4.2). We also investigate whether scale height differences affect the SFE and discuss implications for the scale of physical processes that are important for setting the molecular fraction and the SFE. We examine our results in light of recent star formation models such as the the mid-plane pressure model and the model of Krumholz et al. (2009) (Sections 4.3 and 4.4). To carry out this study, we trace molecular gas with CO(1–0) data from the Institut de Radioastronomie Millimétrique (IRAM) 30 m telescope and atomic gas with H I 21 cm data from the Very Large Array (VLA; Watson et al. 2011, hereafter Paper I). We trace the SFR with H $\alpha$  data from the 2.4 m Hiltner Telescope of the MDM Observatory combined with polycyclic aromatic hydrocarbon (PAH) emission data derived from *Spitzer Space Telescope* Infrared Array Camera (IRAC) observations. We also estimate the stellar mass from the *Spitzer* IRAC data. These observations, and measurements derived from the data, are described in Section 2. We describe the quantities that we derive from these measurements in Section 3. Our results are in Section 4 and we discuss these results in Section 5.

## 2. SAMPLE SUMMARY, OBSERVATIONS, DATA REDUCTIONS, AND MEASUREMENTS

Our sample is composed of 20 Sd-Sdm galaxies within 32 Mpc, with circular velocities between 46 and  $190 \text{ km s}^{-1}$ . These properties are well matched to the Dalcanton et al. (2004) sample. However, in contrast to the Dalcanton et al. (2004) sample of edge-on galaxies, we selected our galaxies to be moderately inclined, with inclinations between  $16^\circ$  and  $56^\circ$ , such that we can accurately measure the SFR and gas surface densities and place the galaxies on the star formation law. Section 2 in Paper I and Table 1 provide a description of the sample selection.

Many of the measurements described in this section were carried out to derive surface densities – of gas, SFR, and stars. These surface densities must be measured over the same area. The IRAM CO(1–0) data are the limiting factor, as they are single-beam,  $\text{FWHM} = 21''$  measurements centered on each galaxy. Therefore, we measured the emission within a  $21''$ -diameter circular aperture centered on the IRAM pointing center, the coordinates of which are listed in Table 2, for the following datasets: the H I data from the VLA, the H $\alpha$  data from the MDM Observatory, and the PAH and  $4.5 \mu\text{m}$  data from *Spitzer* IRAC.

### 2.1. IRAM 30 m CO(1–0)

Thirteen of our objects were observed in the CO(1–0) and CO(2–1) lines at 115 and 230 GHz in May 2007 with the IRAM 30 m telescope on Pico Veleta. Dual polarization receivers were used at both frequencies with the  $512 \times 1$  MHz filterbanks on the CO(1–0) line and the  $256 \times 4$  MHz filterbanks on the CO(2–1) line. The observations were carried out in wobbler switching mode with a wobbler throw of  $200''$  in the azimuthal direction. At

the beginning of the observations the frequency tuning was checked by observing a bright galaxy at a similar redshift. Observations of the same calibration source on different days allowed us to check the relative calibration, which was excellent (better than 10%) for CO(1–0). The calibration in CO(2–1) was equally good, except for one day when the calibration observation was different by  $\sim 35\%$ . Pointing was monitored on nearby quasars, Mars, or Jupiter every 60 – 90 minutes. During the observation period, the weather conditions were generally good, with pointing better than  $3''$ . The typical system temperature was 300–500 K at 115 GHz and 500–1000 K at 230 GHz on the  $T_{\text{A}}^*$  scale. At 115 GHz (230 GHz), the IRAM forward efficiency,  $F_{\text{eff}}$ , was 0.95 (0.91), the beam efficiency,  $B_{\text{eff}}$ , was 0.75 (0.54), and the half-power beam size is  $21''$  ( $11''$ ). All CO spectra and line intensities are presented on the main beam temperature scale ( $T_{\text{mb}}$ ) which is defined as  $T_{\text{mb}} = (F_{\text{eff}}/B_{\text{eff}}) \times T_{\text{A}}^*$ . For the data reduction, we selected the observations with good quality (taken during satisfactory weather conditions and showing a flat baseline), averaged the spectra from the individual scans of the source, and subtracted a constant continuum for the CO(1–0) spectra and a linear continuum for the CO(2–1) spectra.

Figure 1 shows the CO spectra for the objects observed in May 2007. The black spectrum shows the CO(1–0) data and the red spectrum shows the CO(2–1) data. We did not use the CO(2–1) data in this paper, but show it for completeness and to corroborate some of the weaker CO(1–0) detections. The solid black horizontal line is the velocity range over which we integrated to derive the CO(1–0) line intensity. The dashed horizontal line is centered on the systemic velocity of the galaxy, derived from velocity field modeling of our H I emission line data. The width of the dashed line is the width of the H I emission line at 20% of the peak flux density ( $W_{20}$ ; see Table 1 for these values). The integrated CO(1–0) line intensities are presented in Table 2.

We did not detect ESO 544-G03, ESO 418-G008, ESO 501-G023, or UGC 6446. For these galaxies, we quoted the CO line intensities as upper limits, computed with  $I_{\text{CO}} < 3 \sigma_{\text{rms}} (W_{20} \Delta v)^{1/2}$ , where  $\sigma_{\text{rms}}$  is the noise in the spectrum in K and  $\Delta v$  is the CO(1–0) spectrum channel width, which is  $10 \text{ km s}^{-1}$  in the Hanning-smoothed spectra of Figure 1.

CO(1–0) and CO(2–1) spectra and line intensities for six of our objects – PGC 3853, NGC 2805, NGC 3906, NGC 4519, NGC 5964, and NGC 6509 – were presented in Böker et al. (2003), also based on IRAM 30 m observations and reduced in the same manner. We did not obtain CO data for ESO 555-G027.

## 2.2. VLA HI

### 2.2.1. Integrated H I Line Intensity

The H I 21 cm data for our sample were obtained from the VLA/Expanded VLA, operated by the National Radio Astronomy Observatory<sup>8</sup>, for projects AZ0133 (carried out in 2001 August), AL0575 (carried out in 2002 June and November), AM0873 (carried out in 2006 October and November), and AM0942 (carried out in 2008

<sup>8</sup> The National Radio Astronomy Observatory is a facility of the National Science Foundation operated under cooperative agreement by Associated Universities, Inc.

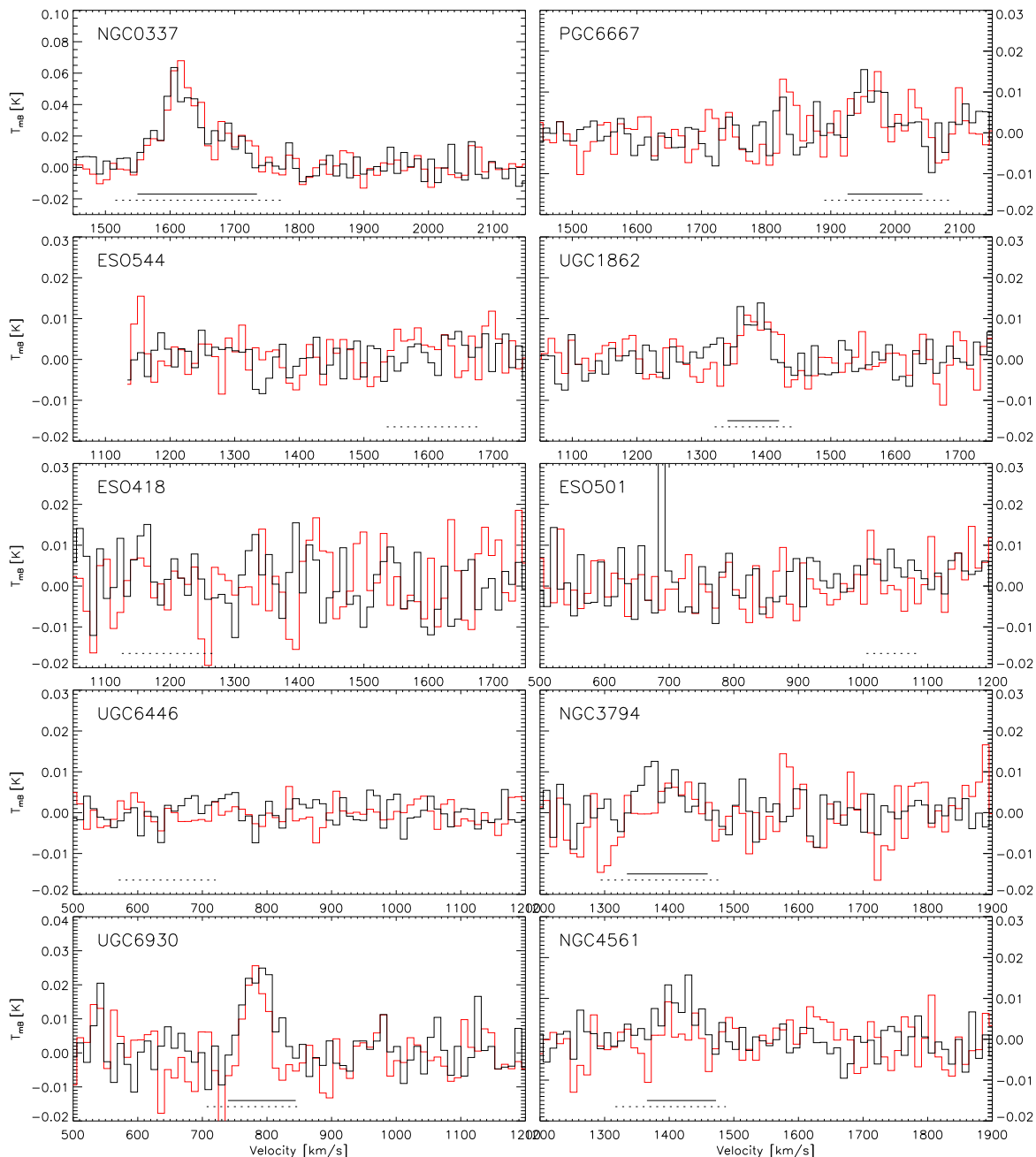


FIG. 1.— CO(1–0) (black) and CO(2–1) (red) spectra for the objects observed in May 2007. See Böker et al. (2003) for the remaining spectra. The black horizontal line designates the velocity range over which we integrated to derive the CO(1–0) line intensity. ESO 544-G03, ESO 418-G008, ESO 501-G023, and UGC 6446 do not have this line because they were undetected. The dashed horizontal line is centered on the systemic velocity derived from velocity field modeling of our H I data, and has a width of  $W_{20}$ , which we derived from the integrated H I line profile.

May and 2009 July and August). The galaxies were observed in the C or CnB configurations, which provide a nominal angular resolution of  $13''$ . The channel width is generally  $5.2 \text{ km s}^{-1}$ . The observations and reductions are described further in Paper I. We measured the integrated H I line intensity from velocity-integrated intensity maps (with units of  $\text{Jy beam}^{-1} \text{ km s}^{-1}$ ) created from naturally-weighted data cubes. The beam major axis FWHM ( $B_{\text{maj}}$ ) and minor axis FWHM ( $B_{\text{min}}$ ) for each data cube are listed in Table 3 of Paper I.

Ten of our objects have  $B_{\text{maj}}$  and  $B_{\text{min}} < 21''$ . To adjust the H I beam to match the CO(1–0) beam, we

used the AIPS task CONVL to convolve the integrated intensity map so the output Gaussian beam has  $B_{\text{maj}} = B_{\text{min}} = 21''$ . To approximately match the H I beam to the CO(1–0) beam for the remaining ten objects with  $B_{\text{maj}} > 21''$  (on average,  $B_{\text{maj}} = 29''$ ) and  $B_{\text{min}} < 21''$ , we either used the original integrated intensity map or convolved the map to have  $B_{\text{min}} = 21''$  and the beam major axis approximately equal to the original  $B_{\text{maj}}$ .

Using the resulting maps, we measured the average H I line intensity in  $\text{Jy beam}^{-1} \text{ km s}^{-1}$  within the  $21''$ -diameter circular aperture ( $\langle I_{\text{HI}} \rangle$ ) with the AIPS task IMEAN. These values are listed in Table 2. The inte-

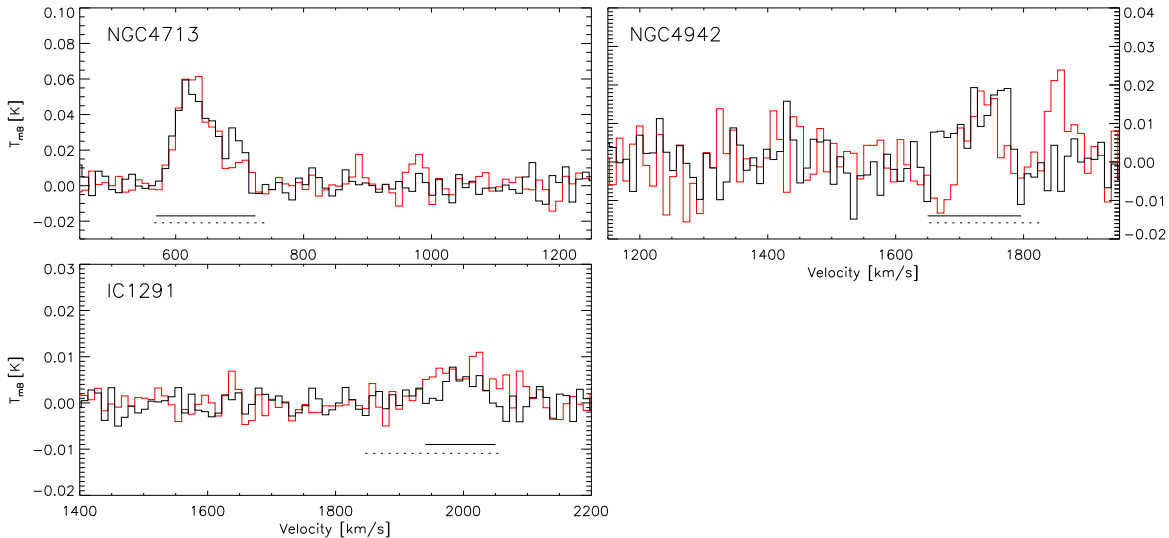


FIG. 1.— (Continued)

grated H I line intensity in  $\text{K km s}^{-1}$  is given by:

$$\langle I_{\text{HI}} \rangle [\text{K km s}^{-1}] = \frac{6.07 \times 10^5 \langle I_{\text{HI}} \rangle [\text{Jy beam}^{-1} \text{ km s}^{-1}]}{B_{\text{maj}} B_{\text{min}}}, \quad (1)$$

where  $B_{\text{maj}}$  and  $B_{\text{min}}$  are in arcseconds and now refer to the beam of the map on which we made the measurements. These values are listed in Table 2.

For the objects with  $B_{\text{maj}} > 21''$ , we assumed that the average line intensity within a  $21''$  beam is equal to the measured line intensity from our image with a larger beam. We estimated the uncertainty introduced by this assumption by convolving the integrated intensity maps of three objects with  $B_{\text{maj}} < 21''$  such that the convolved beams match those of the ten objects with  $B_{\text{maj}} > 21''$ . We measured the average line intensity within the  $21''$ -diameter circular aperture and compared this to the true value measured from the map with a  $21''$  beam. We found that the line intensities in our test cases differ from the true values by up to 11% (in the case of the NGC 4519 beam, which has a  $B_{\text{maj}} = 51.91''$ ) and by 4% on average. The test measurements both over and under estimate the true value depending on the emission distribution. Therefore, we included this in our uncertainty estimate, but make no correction.

The main contributors to the final uncertainty in our H I line intensities are flux calibration (5%), aliasing (up to 11% and described in Paper I), and using an image with a beam larger than  $21''$  to estimate the line intensity within  $21''$  (on average 4%). Not all objects are subject to the latter two uncertainties. Nonetheless, we conservatively assigned the quadrature sum of these uncertainties (13%) as the generic uncertainty associated with our H I line intensities within the  $21''$ -diameter aperture.

NGC 6509 shows H I in absorption on the east side of the galaxy because it is in the foreground of the radio source 4C +06.63. The average line intensity within  $21''$  is unaffected because the eastern edge of the aperture and the western edge of the radio lobe are separated by about  $20''$ .

### 2.2.2. Epicyclic Frequency

We calculated a representative epicyclic frequency ( $\kappa$ ) for the  $21''$ -diameter circular aperture to use in the stability analysis of Section 4.3. We used  $\kappa = \sqrt{2(1 + \beta)} (v/r)$ , where  $\beta = d \log(v) / d \log(r)$ . We determined  $\beta$  and the rotation velocity,  $v$ , at a radius,  $r$ , of  $5.25''$  (half the radius of the  $21''$ -diameter aperture) from the H I rotation curves presented in Paper I, where we fit a tilted ring model to the data to derive  $v$  at radii every  $(B_{\text{maj}} B_{\text{min}})^{0.5}$ , beginning at  $(B_{\text{maj}} B_{\text{min}})^{0.5} / 2$ . We simply fit a line between the origin and the first point in the rotation curve, the average radius of which is  $8.3''$ . We used the slope of the line as an estimate of  $dv/dr$  and evaluated  $v$  at  $5.25''$ . There may be inaccuracies introduced to  $\kappa$  evaluated in this manner because the origin and first point in the rotation curve are within a single beam. Therefore, we also calculated the epicyclic frequency at  $10.5''$  using the same method as above, but by fitting the line between the first and second points from the rotation curve, where the average second radius is  $25.0''$ . The epicyclic frequencies calculated at  $10.5''$  are smaller than the values at  $5.25''$  by 30% on average. We used the epicyclic frequencies evaluated at  $5.25''$  in our stability analysis (and list these in Table 4), but include 30% uncertainties on the values. Beam smearing, where many velocity components are within the spatial beam, is likely in effect in this region. Beam smearing leads to underestimated velocities and gradients (Swaters 1999) and therefore  $\kappa$  may also be underestimated. To account for this, we use  $\kappa$  evaluated at  $5.25''$ , as these values are larger.

### 2.3. MDM H $\alpha$

H $\alpha$  and continuum images of the galaxies were obtained at the MDM 2.4m Hiltner telescope over the course of four observing runs in January 2007, November 2007, May/June 2007, and January 2008. Each galaxy was observed for between 30 min and 2.5 hours through a pair of matched, custom-made 15 nm wide narrow-band filters centered at 663 nm and 693 nm, hereafter the 663bp15 and 693bp15 filters, respectively. The H $\alpha$  emis-

sion line falls within the 663bp15 bandpass for all of the galaxies in this sample. Observations were obtained with the Direct CCD camera “Echelle,” which has 2048x2048 pixels. The CCD was binned over 2x2 pixels to produce a plate scale of 0.55”/pixel, which was well-matched to the 1” – 1.5” image quality measured on most nights. The field of view was 9.4’. Conditions were photometric for most of the observations and a series of spectrophotometric standards were observed for flux calibration, as were a series of twilight flats. The exposure times and observation dates are listed in Table 3.

Overscan subtraction, flat fielding, cosmic ray rejection, and bad pixel removal were performed with IRAF<sup>9</sup>. All of the 663bp15 and 693bp15 images of each galaxy were registered to a common coordinate system with SCAMP (Bertin 2006) and a combined image for each filter was constructed with SWARP (Bertin et al. 2002).

Observations of spectrophotometric standard stars were used to determine the absolute flux calibration for the 663bp15 filter (including an airmass correction) and the relative throughput of the two filters. We calculated the expected ratio of stellar flux in these filters for late-type galaxies by using the SYNPHOT package in IRAF to convolve the filter transmission functions with a series of Bruzual & Charlot 1995 (e.g., Bruzual & Charlot 2003) stellar population synthesis models with both continuous and exponentially declining ( $\tau = 1$  Gyr) star formation histories. The range of flux ratios from these models and the relative throughput of the two filters were used to scale the 693bp15 image and subtract it from the 663bp15 image to create an H $\alpha$  image for each galaxy.

We measured the H $\alpha$  flux for each galaxy within the 21”-diameter circular aperture and within a circle of diameter  $D_{25}$ , the B-band major isophotal diameter at 25 mag arcsec<sup>-2</sup>, with aperture photometry. All H $\alpha$  flux measurements were multiplied by a factor of 0.75 to account for emission from [N II]  $\lambda\lambda 6548, 6584$  in the 663bp15 bandpass (Kennicutt 1983). The H $\alpha$  flux measurements were also corrected for Galactic extinction using the extinction law of O’Donnell (1994) assuming  $R_V = 3.1$  and reddening values from Schlegel et al. (1998) and tabulated on NED<sup>10</sup>. The final values within the 21” aperture are listed in Table 2.

A number of our galaxies show substantial variation in the H $\alpha$  flux within the 21” aperture if we vary the center of the aperture by the  $\sim 2 - 3$ ” pointing accuracy of the IRAM 30m. Including this uncertainty, as well as uncertainty in the [NII] correction and absolute calibration uncertainties, we estimate the uncertainty in the H $\alpha$  flux within the 21”-diameter aperture to be about 30%.

Figure 2 compares our H $\alpha$  fluxes measured within  $D_{25}$  relative to published values from Koopmann et al. (2001), James et al. (2004), Moustakas & Kennicutt (2006), and Epinat et al. (2008), where we corrected the published values for [N II] emission and Galactic extinction if necessary. Our values are on average 20% smaller

<sup>9</sup> IRAF is distributed by the National Optical Astronomy Observatory, which is operated by the Association of Universities for Research in Astronomy (AURA) under cooperative agreement with the National Science Foundation.

<sup>10</sup> The NASA/IPAC Extragalactic Database (NED) is operated by the Jet Propulsion Laboratory, California Institute of Technology, under contract with the National Aeronautics and Space Administration.

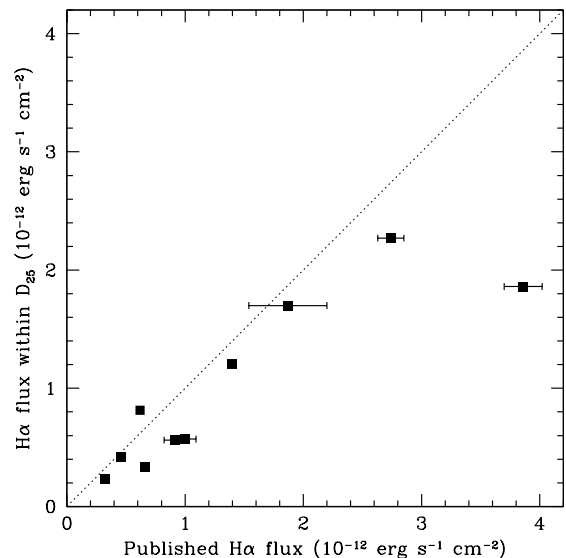


FIG. 2.— Comparison between our H $\alpha$  fluxes measured within a circle of diameter  $D_{25}$  and published H $\alpha$  fluxes. Both values are corrected for [N II] emission and Galactic extinction. The dotted line shows equality. The largest outlier is NGC 0337.

than the published values. This systematic offset is comparable to our calibration uncertainty and may be due to differences in the filter profiles, the angular extent of the apertures, and the treatment of bright stars with potentially large subtraction residuals. We note that this offset corresponds to an uncertainty in the star formation rate surface density of less than 0.1 dex, which is smaller than the 0.2 dex uncertainty that we assign due to the variable contribution to dust heating from non-star forming populations.

#### 2.4. *Spitzer* IRAC

Fourteen of the 20 galaxies were observed as part of our *Spitzer* Cycle 5 Program 50102; the remaining six (NGC 337, UGC 1862, ESO 418-G008, NGC 2805, NGC 4519, and NGC 4561) were observed for various other programs. Observations for Program 50102 consisted of five, dithered observations with a frame time of 30s in all four IRAC channels (3.6  $\mu$ m, 4.5  $\mu$ m, 5.8  $\mu$ m, and 8  $\mu$ m). Data for the other six archival datasets were comparable to our observations, with the exception that the data for UGC 1862 only include the galaxy in channels 2 and 4. In the analysis described below, we use the channel 1, 2 and 4 data.

The Basic Calibrated Data (BCD) for all 20 galaxies were processed with Sean Carey’s artifact mitigation software<sup>11</sup>, which corrects for a variety of effects such as muxbleed, column pulldown/pullup, electronic banding, and first frame effect. We then created mosaics for each channel with the *Spitzer Science Center’s* MOPEX (MOasicker and Point source EXtractor) package. This package corrects individual images for background variations and optical distortions, and then projects them onto an output mosaic image for each channel. These

<sup>11</sup> [http://spider.ipac.caltech.edu/staff/carey/irac\\_artifacts/](http://spider.ipac.caltech.edu/staff/carey/irac_artifacts/)

mosaic images were used for five measurements for each galaxy: the inclination ( $i$ ), position angle of the major axis (PA), the PAH flux density, the  $4.5\ \mu\text{m}$  flux density, and the exponential disk scale length.

#### 2.4.1. Inclination and Position Angle

We estimated the inclination and PA for each galaxy with the IRAF `ellipse` task, which fits elliptical isophotes with the iterative method described by Jedrzejewski (1987). The  $3.6\ \mu\text{m}$  data ( $4.5\ \mu\text{m}$  for UGC 1862) were fit because this channel has the greatest sensitivity to the old stellar population, yet is relatively insensitive to dust.

We found that the isophote fits, particularly in the outer, low-surface brightness regions, were relatively sensitive to the presence of bright stars. We therefore created masks of these stars with the SExtractor package (Bertin & Arnouts 1996) and included this mask as an input to the `ellipse` task. These masks also excluded regions with relatively poor coverage in the IRAC mosaic. We averaged the PA and ellipticity values for the largest isophotes to derive our final PAs and inclinations. These values were used as inputs for the rotation curve analysis described in Paper I and were reported in Table 5 of that work.

#### 2.4.2. PAH Flux Density

We calculated the PAH flux density within the  $21''$ -diameter circular aperture using the  $8\ \mu\text{m}$  images, which are dominated by the  $7.7$  and  $8.6\ \mu\text{m}$  PAH features, and the stellar emission-dominated  $3.6\ \mu\text{m}$  images. We measured the  $8\ \mu\text{m}$  and  $3.6\ \mu\text{m}$  flux densities using the IRAF task `phot`. In both measurements, we subtracted from each pixel the median sky background, which we measured within a large-radius annulus centered on the galaxy. We applied the band-specific extended source aperture correction to the  $8\ \mu\text{m}$  and  $3.6\ \mu\text{m}$  flux densities (described in the IRAC Instrument Handbook; for the  $21''$ -diameter circular aperture, the correction is 0.985 and 0.896 for the  $3.6\ \mu\text{m}$  and  $8\ \mu\text{m}$  bands, respectively). Finally, the PAH flux density is the  $8\ \mu\text{m}$  flux density, less the stellar emission contribution, which we estimated by scaling the  $3.6\ \mu\text{m}$  flux density by 0.255 (as used in Kennicutt et al. 2009). For UGC 1862, we used the  $4.5\ \mu\text{m}$  flux density, scaled by a factor of 0.389, to remove the stellar contribution to the  $8\ \mu\text{m}$  band. This scale factor is derived from values quoted in Helou et al. (2004), except we assumed that all the  $4.5\ \mu\text{m}$ -band emission is stellar. The uncertainties on the calibrated  $3.6\ \mu\text{m}$  and  $8\ \mu\text{m}$  flux densities are about 10% (Hora et al. 2004). We quote PAH flux density uncertainties that are simple error propagated values. Our PAH flux densities are presented in Table 2.

#### 2.4.3. $4.5\ \mu\text{m}$ Flux Density

We calculated the total  $4.5\ \mu\text{m}$  flux density and the flux density within the  $21''$ -diameter circular aperture such that we can derive the total stellar mass and the stellar mass surface density in Section 3.3. We first masked out bright foreground stars with the IRAF APPHOT and DAOPHOT packages, in particular the `phot` and `substar` tasks. We used large  $4.5\ \mu\text{m}$  to  $8.0\ \mu\text{m}$  flux ratios to identify foreground stars. For a few bright stars

that were not adequately subtracted, we manually replaced the affected pixels with values from a region at a similar radius from the center of the galaxy.

We used the IRAF task `phot` to measure the flux density within the  $21''$ -diameter circular aperture. For the total flux density, we used the IRAF task `ellipse` to measure the flux density within an ellipse where the semi-major axis (SMA) is  $D_{25}/2$  and the PA and ellipticity ( $e = 1 - \cos i$ ) were derived from a combination of rotation curve analyses on the VLA H I data and the ellipse fits of the IRAC  $3.6\ \mu\text{m}$  data, described in Section 2.4.1 (PA and  $i$  are given in Table 1). In both measurements, we subtracted the median sky background from each pixel, measured within a large-radius annulus centered on the galaxy.

To confirm that the  $D_{25}$  aperture is appropriate for the total flux density measurement, we identified the SMA where the surface brightness profile flattens (specifically, where the surface brightness decreases by, on average, less than 2% over a number of apertures). The flux density enclosed within this ellipse was generally within 7% of the flux density within the  $D_{25}$  ellipse, except in two cases: UGC 6446 and UGC 6930, where the flux density within the  $D_{25}$  ellipse was larger by a factor of 1.9 and 1.5, respectively. We henceforth use the flux density within the  $D_{25}$  ellipse as the total flux density.

We applied the extended source aperture correction to the  $21''$  and  $D_{25}$  flux density measurements, with a value of 1.013 for the  $21''$  aperture and an average value of 0.944 for the  $D_{25}$  measurements. We did not apply a color correction. The  $21''$  and total  $4.5\ \mu\text{m}$  flux densities are listed in Table 2.

#### 2.4.4. Exponential Disk Scale Length

We estimated the exponential scale length of each galaxy using the IRAF `ellipse` task on the  $4.5\ \mu\text{m}$  data, allowing the center, PA, and ellipticity to vary as a function of semi-major axis. We fit an exponential to the mean isophotal intensity profile to derive the central surface brightness and scale length. We excluded PSF and/or bar components from the profile fit based on visual examination of the images and a provisional GALFIT (Peng et al. 2002) analysis. We created a two-dimensional image representing the `ellipse` profile with `bmodel`, subtracted the model from the original image, and found that the standard deviation in the region of the galaxy within the residual image is typically less than about ten times the standard deviation in a galaxy-free region of the original image. Given the small-scale structures present in most of the galaxies, we accepted these values and fits. The scale lengths are listed in Table 4 and are between 0.69 and 3.4 kpc.

We assigned an error of 20% to the scale lengths, based on comparing the scale lengths computed as described above to scale lengths computed from ellipse runs where we held the PA and ellipticity fixed as a function of semi-major axis at the values from Table 1. We confirmed that scale lengths derived from the  $3.6\ \mu\text{m}$  data are generally consistent with the values derived from the  $4.5\ \mu\text{m}$  data within the uncertainty (they differ by 9% on average).

### 3. DERIVED QUANTITIES

For all the surface density calculations below, we used the  $21''$ -diameter aperture, to match the beam of our

CO(1–0) data from IRAM. Table 4 lists the physical size of 21'' (0.7 - 3.2 kpc) and the parameters derived in the following sections. The surface densities are all within the deprojected area of the aperture, which we calculated with the inclinations from Table 1.

### 3.1. Atomic, Molecular, and Total Hydrogen Surface Density

The H I surface density is given by:

$$\Sigma_{\text{HI}} [M_{\odot} \text{ pc}^{-2}] = 0.015 \langle I_{\text{HI}} \rangle \cos(i), \quad (2)$$

where  $\langle I_{\text{HI}} \rangle$  is the average integrated H I line intensity within the 21''-diameter circular aperture in  $\text{K km s}^{-1}$  from Section 2.2.1. We did not include a correction for He. The  $\Sigma_{\text{HI}}$  uncertainty is dominated by the contribution from the line intensity uncertainty and the typical uncertainty in  $\log(\Sigma_{\text{HI}})$  is 0.06 dex. The  $\text{H}_2$  surface density is given by:

$$\Sigma_{\text{H}_2} [M_{\odot} \text{ pc}^{-2}] = 3.2 \frac{X_{\text{CO}}}{2.0 \times 10^{20} \text{ cm}^{-2} (\text{K km s}^{-1})^{-1}} I_{\text{CO}} \cos(i), \quad (3)$$

where  $X_{\text{CO}}$  is the CO-to- $\text{H}_2$  conversion factor and  $I_{\text{CO}}$  is the CO line intensity in  $\text{K km s}^{-1}$  from Section 2.1. We used a constant  $X_{\text{CO}}$  of  $2.8 \times 10^{20} \text{ cm}^{-2} (\text{K km s}^{-1})^{-1}$ . We used this value rather than the Milky Way value of  $2.0 \times 10^{20} \text{ cm}^{-2} (\text{K km s}^{-1})^{-1}$  so we can plot the Kennicutt (1998) total hydrogen star formation law relative to our data. Again, we did not include a correction for He.

The typical uncertainty in  $\log(\Sigma_{\text{H}_2})$  is 0.07 dex, due mainly to the CO line intensity uncertainty. We did not include uncertainty due to  $X_{\text{CO}}$ . Leroy et al. (2011) studied five local group galaxies and concluded that  $X_{\text{CO}}$  is relatively constant at the solar value for  $12 + \log(O/H) \gtrsim 8.4$  and increases with decreasing oxygen abundance below  $12 + \log(O/H) \sim 8.2 - 8.4$ . We have only one galaxy where we estimated that the oxygen abundance is below  $12 + \log(O/H) = 8.4$  (Section 3.3), so we do not expect much  $X_{\text{CO}}$  variation in our sample.

We also use the total hydrogen surface density,  $\Sigma_{\text{HI}+\text{H}_2} = \Sigma_{\text{HI}} + \Sigma_{\text{H}_2}$ . The typical uncertainty in  $\log(\Sigma_{\text{HI}+\text{H}_2})$  is 0.05 dex.

### 3.2. Star Formation Rate Surface Density

We used  $\text{H}\alpha$  emission to trace the unobscured SFR and PAH emission to trace the obscured SFR. The  $\text{H}\alpha$  emission is due to recombination in H II regions, which are ionized by O and early B stars. PAHs are small dust grains (or large molecules) that are primarily excited by single UV photons (Sellgren 1984; Leger & Puget 1984). Because ionizing radiation is not required to heat PAHs (and in fact there is evidence that ionizing radiation destroys PAHs; Helou et al. 2004; Peeters et al. 2004), PAH emission traces lower-mass, longer-lived stars than those ultimately responsible for the  $\text{H}\alpha$  emission. PAH emission has been used to trace the total SFR (e.g., Zhu et al. 2008), but there is variation in the  $8 \mu\text{m}$  luminosity at a given SFR due to environment, especially metallicity (e.g., Calzetti et al. 2007). Kennicutt et al. (2009) used 75 galaxies to calibrate SFR estimates based on  $\text{H}\alpha$  and PAH emission by comparing the combined

$\text{H}\alpha$  and PAH luminosity to the  $\text{H}\alpha$  luminosity corrected for extinction using the Balmer decrement. The authors found that SFRs calculated with  $\text{H}\alpha$  and PAH emission agreed with their reference SFRs with as little scatter as SFRs calculated with  $\text{H}\alpha$  and  $24 \mu\text{m}$  emission. We used the SFR calibration of Kennicutt et al. (2009) to calculate the SFR surface density within the 21''-diameter circular aperture:

$$\Sigma_{\text{SFR}} [M_{\odot} \text{ yr}^{-1} \text{ kpc}^{-2}] = 7.30 \times 10^{10} (F_{\text{H}\alpha} + 1.1 \times 10^{-28} \nu F_{\text{PAH}}) \cos(i), \quad (4)$$

where  $F_{\text{H}\alpha}$  and  $F_{\text{PAH}}$  are the  $\text{H}\alpha$  flux in  $\text{erg s}^{-1} \text{ cm}^{-2}$  and the PAH flux density in mJy within the 21''-diameter circular aperture,  $\nu$  is the central frequency of the  $8 \mu\text{m}$  IRAC band in Hz, and the constant includes the aperture area. This assumes the initial mass function (IMF) from Calzetti et al. (2007), which is similar to that presented in Kroupa (2001). The Kennicutt et al. (2009) SFR was calibrated for galaxy-averaged data, but should be appropriate for our data because we generally probe regions that are a couple of square kpc in area and should therefore contain a number of star forming regions. Even using both  $\text{H}\alpha$  and PAHs to trace the SFR, galaxies with low metallicity could have underestimated SFRs because the fraction of dust mass in PAHs decreases at low metallicity, particularly below  $Z_{\odot}/4$  ( $12 + \log(O/H) \lesssim 8.3$ ; Draine et al. 2007; Smith et al. 2007). In the following section we estimate the oxygen abundance of each galaxy from the stellar mass and find that only one galaxy (ESO 501-G023) has  $12 + \log(O/H) < 8.3$ . Therefore, we do not expect significant SFR underestimates in our sample.

Kennicutt et al. (2009) discussed that the dominant source of uncertainty in their SFRs is due to varying contributions to dust heating from older stellar populations ( $\gtrsim 100$  Myr). Based on their suggestions, and including the fact that our sample has a limited range in morphology and therefore star formation history, we assigned a general uncertainty of 0.2 dex to our SFR surface densities. This dominates over the contribution due to  $\text{H}\alpha$  flux and PAH flux density measurement uncertainties.

In upcoming sections, we use the SFE defined as  $\Sigma_{\text{SFR}}/\Sigma_{\text{HI}+\text{H}_2}$  in  $\text{yr}^{-1}$ . The typical uncertainty in the SFE is 0.2 dex.

### 3.3. Stellar Mass Surface Density, Total Stellar Mass, and Oxygen Abundance

We derived the stellar mass surface density within the 21''-diameter circular aperture and the total stellar mass from the  $4.5 \mu\text{m}$  flux densities. We chose to use the  $4.5 \mu\text{m}$  data over the  $3.6 \mu\text{m}$  data because there are no PAH emission features in the  $4.5 \mu\text{m}$  band.

To estimate the stellar mass, we used a relationship between K-band mass-to-light ratio and color from Bell & de Jong (2001), derived from stellar population synthesis modeling:

$$\log(\Upsilon_*^{\text{K}}) = 1.43(J - K_s) - 1.53, \quad (5)$$

where  $\Upsilon_*^{\text{K}}$  is the mass-to-light ratio in the K band in  $M_{\odot}/L_{\text{K},\odot}$ ,  $L_{\text{K},\odot}$  is the solar luminosity in the K band, and the  $J$  and  $K_s$  magnitudes are from the Two Micron All Sky Survey (2MASS; mainly the Extended Source Catalog, but three galaxies are in the Large Galaxy Atlas



of Jarrett et al. 2003) and are listed in Table 2. The original relationship uses Johnson  $K$  magnitudes, but use of  $K_s$  magnitudes does not introduce significant error to the mass. This relation is a linear combination of the  $\Upsilon_*^K - (V - J)$  and  $\Upsilon_*^K - (V - K)$  relations presented in Table 1 of Bell & de Jong (2001) and we subtracted 0.15 dex to convert from the scaled Salpeter IMF that the authors use to a Kroupa (2001) IMF. For three galaxies that do not have 2MASS data, we used:

$$\log \Upsilon_*^K = 0.21(B - K_s) - 1.11 = 0.21(B - [4.5]) - 1.23, \quad (6)$$

where we used B-band magnitudes from the Third Reference Catalogue of Bright Galaxies (RC3; de Vaucouleurs et al. 1991, also listed in Table 1). This equation is similar to that used in Lee et al. (2006), but we used the Bell & de Jong (2001) Table 1 model results, we have converted to a Kroupa (2001) IMF, and we assumed  $(K_s - [4.5]) = 0.58$ . This color is the average value from the eleven galaxies in our sample where the 2MASS aperture radius (“r\_m\_ext”) and our aperture SMA ( $D_{25}/2$ ) differ by less than 40% of our SMA. Six galaxies have spuriously large/red ( $K_s - [4.5]$ ) colors because the 2MASS aperture radius is much smaller than our aperture radius (as small as 20% of our aperture radius; for a similar effect, see Dale et al. 2009).

We then calculated the stellar mass within the 21''-diameter circular aperture and the total stellar mass with:

$$\log(M_*/M_\odot) = \log \Upsilon_*^K + \log(L_{4.5}/L_{4.5,\odot}) - 0.4(K_s - [4.5]), \quad (7)$$

as in Lee et al. (2006). To calculate the luminosity of the galaxy,  $L_{4.5}$ , we used either the  $4.5 \mu\text{m}$  flux density within the 21''-diameter circular aperture or the total  $4.5 \mu\text{m}$  flux density from Table 2, the distances presented in Table 1, the absolute  $4.5 \mu\text{m}$  magnitude of the Sun,  $M_{4.5,\odot} = 3.3$  (Lee et al. 2006; Oh et al. 2008), and the zero-magnitude flux density of the  $4.5 \mu\text{m}$  band,  $F_{4.5}^0 = 179.7 \text{ Jy}$  (Reach et al. 2005). This equation uses the fact that  $(K - [4.5]) \sim 0$  for the Sun. We again assumed  $(K_s - [4.5]) = 0.58$ , for all galaxies in this case. For the stellar mass surface density ( $\Sigma_*$ ), we then divided by the deprojected area of the 21''-diameter circular aperture.

The average offset between masses computed with Equations 5 and 6 is 0.2 dex, with masses computed with Equation 6 generally smaller. This offset is smaller than our estimate of the uncertainty in the mass, described further below. The masses computed with Equation 7 above are in good agreement with masses computed using the Oh et al. (2008) relationship between K-band and  $4.5 \mu\text{m}$  band mass-to-light ratios, derived from stellar population synthesis modeling.

Bell & de Jong (2001) cite uncertainties of 0.1–0.2 dex in their mass-to-light ratios, which includes model and dust uncertainties and allows for small star formation bursts. The uncertainty introduced to the stellar mass by uncertainties in  $L_{4.5}$  is of similar order, mainly due to distance uncertainties. We assigned a general uncertainty of 0.3 dex to the stellar masses, which is the quadrature sum of the above uncertainties. This is in agreement with the Conroy et al. (2009) estimate of typical stellar mass uncertainties from stellar population synthesis modeling. The uncertainty in the stellar mass sur-

face density is dominated by the contribution from the mass-to-light ratio. We therefore assigned a typical uncertainty of 0.2 dex.

We estimated a representative oxygen abundance for each galaxy to help assess the accuracy and precision of our molecular hydrogen and SFR surface densities (Sections 3.1 and 3.2) and also so we can compare our data to the Krumholz et al. (2009) model (Section 4.4). We estimated the oxygen abundance with the total stellar masses calculated from the  $4.5 \mu\text{m}$  flux density and the mass-metallicity relation of Tremonti et al. (2004) (their Equation 3), which assumes a Kroupa (2001) IMF, consistent with the rest of our analysis. We derive an average uncertainty in  $12 + \log(O/H)$  of 0.11 dex.

#### 3.4. Stability Parameters and Mid-Plane Pressure

In Section 4.3, we study trends between SFE and stability, parametrized by a generalized Toomre  $Q$  parameter (Toomre 1964; Rafikov 2001). We calculated the stability parameters within the 21''-diameter circular aperture. The stability parameter for the gas and stellar components of the disk are

$$Q_{\text{gas}} = \frac{\kappa \sigma_{\text{gas}}}{\pi G \Sigma_{\text{gas}}}, \text{ and} \quad (8)$$

$$Q_{\text{stars}} = \frac{\kappa \sigma_{*,r}}{\pi G \Sigma_*}, \quad (9)$$

respectively, where  $\kappa$  is the epicyclic frequency and  $\sigma_{\text{gas}}$  and  $\sigma_{*,r}$  are the gas and radial stellar velocity dispersions. Rafikov (2001) calculated the stability parameter that includes both gas and stars in a thin rotating disk:

$$\frac{1}{Q_{\text{gas+stars}}} = \frac{2}{Q_{\text{stars}}} \frac{q}{1+q^2} + \frac{2}{Q_{\text{gas}}} R \frac{q}{1+q^2 R^2}, \quad (10)$$

where  $q = \kappa \sigma_{*,r} / \kappa$ ,  $R = \sigma_{\text{gas}} / \sigma_{*,r}$ , and  $k$  is a free parameter that represents the wavenumber of the perturbation. In all cases, the instability condition is when  $Q < 1$  (except, strictly speaking,  $Q_{\text{stars}} < 1.07$ ). Romeo & Wiegert (2011) included disk thickness in the stability estimation by incorporating a factor related to the ratio of the vertical to radial velocity dispersion, but we settled on the Rafikov (2001) parameter for ease of comparison with other works.

We generally made similar assumptions for the components of  $Q$  as Leroy et al. (2008). We assumed  $\sigma_{\text{gas}} = 11 \text{ km s}^{-1}$ , which is appropriate for the warm neutral medium,  $\sigma_{*,r} = 1.67 \sigma_{*,z}$ , and  $\sigma_{*,z} = (2\pi G l_* \Sigma_*/7.3)^{0.5}$ , where  $\sigma_{*,z}$  is the vertical stellar velocity dispersion and  $l_*$  is the stellar scale length (Tamburro et al. 2009; Shapiro et al. 2003; van der Kruit & Searle 1981; van der Kruit 1988). This  $\sigma_*$  equation assumes that the disk is isothermal in the  $z$  direction,  $h_*$  is constant as a function of radius, and  $l_*/h_* = 7.3$  (as observed by Kregel et al. 2002), where  $h_*$  is the stellar scale height. Note that the latter two assumptions are not in conflict with a sample like Dalcanton et al. (2004) because those authors found only a transition in dust scale height with circular velocity, not in stellar scale height. We used the scale lengths and stellar mass surface densities from Sections 2.4.4 and 3.3 to derive  $\sigma_{*,r}$  values between 9 and  $78 \text{ km s}^{-1}$ .

For  $\Sigma_{\text{gas}}$ , we multiplied the total-hydrogen surface density ( $\Sigma_{\text{HI+H}_2}$ ) by a factor of 1.36 to include helium. For

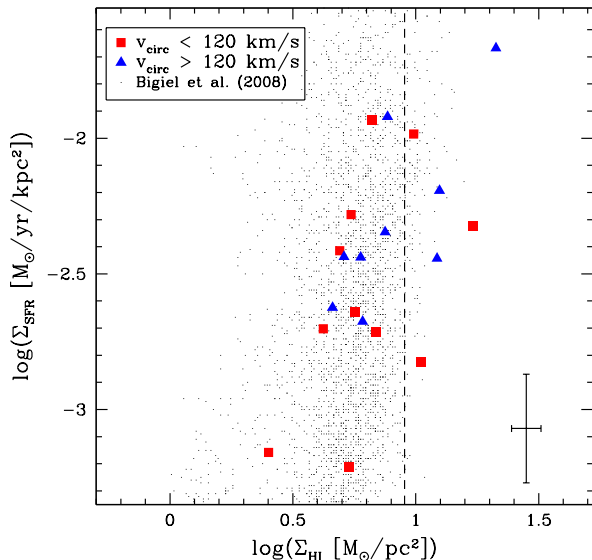


FIG. 3.— SFR surface density versus atomic hydrogen surface density. Red squares represent galaxies with  $v_{\text{circ}} < 120 \text{ km s}^{-1}$ . Blue triangles represent galaxies with  $v_{\text{circ}} > 120 \text{ km s}^{-1}$ . The circular velocities are from H I rotation curve fits (Paper I). A representative error bar is shown in the lower right corner (see Sections 3.1 and 3.2 for details). The vertical dashed line is at  $9 M_{\odot} \text{ pc}^{-2}$ , the typical maximum density for atomic hydrogen. For comparison, the small black points represent measurements from Bigiel et al. (2008) from seven spiral galaxies sampled at 750 pc resolution.

$\Sigma_*$ , we used the value derived in Section 3.3. For the epicyclic frequency, we used the value from Section 2.2.2, evaluated at  $5.25''$ . For the wavenumber of the perturbation,  $k = 2\pi/\lambda$ , where  $\lambda$  is the wavelength of the perturbation, we used the common method of varying  $\lambda$  to find the minimum  $Q_{\text{gas+stars}}$  ( $Q_{\text{gas+stars,min}}$ ) for the region (e.g., Yang et al. 2007; Yim et al. 2011). This typically results in smaller, less stable  $Q_{\text{gas+stars}}$  compared to  $Q_{\text{gas}}$  and  $Q_{\text{stars}}$ . We found  $\lambda = 0.5 - 3.8 \text{ kpc}$  at  $Q_{\text{gas+stars,min}}$ . We propagated the uncertainties in  $\kappa$ ,  $l_*$ ,  $\Sigma_{\text{gas}}$ , and  $\Sigma_*$  to derive a typical uncertainty in  $Q_{\text{gas}}$  of 30%, in  $Q_{\text{stars}}$  of 60%, and in  $Q_{\text{gas+stars}}$  of 40%.

We also calculated the mid-plane pressure ( $P_{\text{h}}$ ) with the following equation from Elmegreen (1989):

$$P_{\text{h}} \approx \frac{\pi}{2} G \Sigma_{\text{gas}} \left( \Sigma_{\text{gas}} + \frac{\sigma_{\text{gas}}}{\sigma_{*,z}} \Sigma_* \right) \quad (11)$$

We propagated the uncertainties in  $l_*$ ,  $\Sigma_{\text{gas}}$ , and  $\Sigma_*$  to derive a typical uncertainty in  $P_{\text{h}}$  of 40%.

## 4. RESULTS

### 4.1. Bulgeless Disk Galaxies on the Kennicutt-Schmidt Law

In this section, we determine whether our galaxy sample follows the various versions of the Kennicutt-Schmidt law, i.e. the relation between the surface density of gas (atomic, molecular, or the sum of both) and SFR (Sections 4.1.1 - 4.1.3). In Section 4.2, we use these results to show that there is no transition in SFE at a circular velocity of  $120 \text{ km s}^{-1}$ , or at any other circular velocity probed by our sample ( $v_{\text{circ}} = 46 - 190 \text{ km s}^{-1}$ ). The

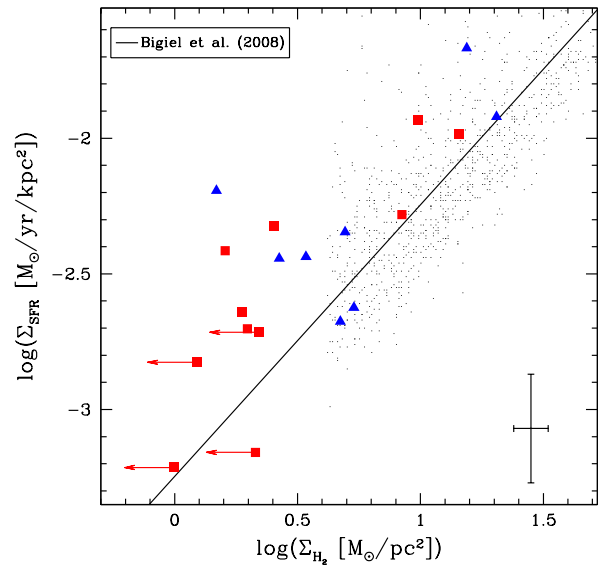


FIG. 4.— SFR surface density versus molecular hydrogen surface density. Symbols are as in Figure 3. The solid line shows the Bigiel et al. (2008) fit to the molecular hydrogen star formation law:  $\Sigma_{\text{SFR}} \propto \Sigma_{\text{H}_2}$ . We discuss the offset of our data relative to this fit in Section 4.1.2.

circular velocities were derived from H I rotation curve fits in Paper I and we include them in Table 1 for convenience.

#### 4.1.1. Atomic Hydrogen Kennicutt-Schmidt Law

Figure 3 shows the relationship between the star formation rate surface density and the atomic hydrogen surface density within the  $21''$ -diameter circular aperture, which corresponds to physical diameters of 0.7 - 3.2 kpc. Red squares denote galaxies with  $v_{\text{circ}} < 120 \text{ km s}^{-1}$  and blue triangles denote galaxies with  $v_{\text{circ}} > 120 \text{ km s}^{-1}$ . The vertical dashed line is at  $9 M_{\odot} \text{ pc}^{-2}$  and represents the typical maximum H I surface density observed in most nearby galaxies (Bigiel et al. 2008). For comparison, we have shown as small dots the 750 pc-diameter regions from the seven spiral galaxies studied in Bigiel et al. (2008) and Leroy et al. (2008). Consistent with our assumptions, Bigiel et al. (2008) used the same Kroupa-type IMF and do not include He in their gas surface densities. An important difference between our datasets is that Bigiel et al. (2008) derived their SFR surface densities from a combination of FUV (1350 - 1750 Å) and  $24 \mu\text{m}$  data while we use H $\alpha$  and PAH emission.

The Spearman rank correlation coefficient for our data is 0.5. For comparison, the coefficient for the Bigiel et al. (2008) data is 0.4. Our data are more correlated than the Bigiel et al. (2008) data, primarily because our sample includes several galaxies with large H I surface densities.

#### 4.1.2. Molecular Hydrogen Kennicutt-Schmidt Law

Figure 4 shows the relationship between the star formation rate surface density and the molecular hydrogen surface density. The symbols are as in Figure 3. We convert the Bigiel et al. (2008)  $\Sigma_{\text{H}_2}$  values to  $X_{\text{CO}} =$

$2.8 \times 10^{20} \text{ cm}^{-2} (\text{K km s}^{-1})^{-1}$  to match our assumptions. The solid line shows the Bigiel et al. (2008) fit, also converted to the above  $X_{\text{CO}}$ . The Spearman rank correlation coefficient for our data is 0.7, including upper limits. For comparison, the coefficient for the Bigiel et al. (2008) data is 0.8.

Our sample of bulgeless disk galaxies, both the low- and high- $v_{\text{circ}}$  objects, appears to lie offset to higher star formation rate surface densities relative to the Bigiel et al. (2008) fit. In what follows, we investigate the significance of and possible reasons for this offset.

Under our assumptions (He not included in the gas surface densities,  $X_{\text{CO}} = 2.8 \times 10^{20} \text{ cm}^{-2} [\text{K km s}^{-1}]^{-1}$ , and the Kroupa-type IMF), the Bigiel et al. (2008) fit is  $\log(\Sigma_{\text{SFR}} [M_{\odot} \text{ yr}^{-1} \text{ kpc}^{-2}]) = a + b \log(\Sigma_{\text{H}_2} [M_{\odot} \text{ pc}^{-2}])$  with  $a = -3.3 \pm 0.2$  and  $b = 1.0 \pm 0.2$ . We fit for the intercept of our data assuming the Bigiel slope of  $b = 1.0$  and including our upper limits in the fit and find  $a = -3.0$  with an rms of 0.3 dex.

We determine the significance of the offset between our sample of bulgeless disk galaxies and the Bigiel et al. (2008) fit to the molecular hydrogen star formation law by randomly selecting nineteen measurements from Bigiel et al. (2008), allowing multiple selections of the same point (Press et al. 1992). We assume a slope of 1.0, calculate the intercept, and repeat this process  $10^6$  times. We find that the probability of measuring a intercept greater than or equal to  $-3.0$  is  $4 \times 10^{-6}$ .

We can exclude two possible reasons for the offset. First, the offset is not likely due to the measurements being central values because we confirmed that the centers of the Bigiel et al. (2008) galaxies are not offset from the general trend (this can also be seen in Figure 10 of Bigiel et al. 2008). Second, our assumption of a single CO-to-H<sub>2</sub> conversion factor probably does not lead to underestimated molecular surface densities because our sample includes only one galaxy for which  $X_{\text{CO}}$  may be underestimated because of a low oxygen abundance, as discussed in Section 3.1. Furthermore, we do not find that galaxies with lower stellar mass, and by implication lower- $(O/H)$ , are more offset from the Bigiel et al. (2008) fit. Note, however, that Schrubba et al. (2011) did observe that lower-oxygen abundance (down to  $12 + \log(O/H) = 8.25$ ) galaxies are offset to higher molecular SFE in their study of 33 galaxies with directly-measured oxygen abundances. They discussed that more observations are needed to determine if the offset is due to  $X_{\text{CO}}$  variation or if it represents true SFE variation.

The quoted Bigiel et al. (2008) intercept uncertainty (0.2 dex) takes into account variations in star formation tracers, uncertainty introduced by estimating the CO(1–0) line intensity from CO(2–1) data, and scatter in the data. The first of these is particularly relevant in comparing our datasets because we trace star formation with H $\alpha$  and PAH data and Bigiel et al. (2008) trace star formation with FUV and  $24 \mu\text{m}$  data. Our intercept is larger than the Bigiel et al. (2008) intercept by only  $1.2\sigma$ , if we take their error bar as  $\sigma$ . In summary, our data are significantly offset from the Bigiel et al. (2008) fit to the molecular hydrogen star formation law in terms of statistical uncertainties, but are nearly consistent if systematic errors are included.

Kennicutt et al. (2007) discussed that offsets are ex-

pected between star formation laws derived from observations at different spatial resolution if the power-law index of the star formation law is not equal to one ( $\Sigma_{\text{SFR}} \propto \Sigma_{\text{gas}}^N$  with  $N \neq 1$ ). In transitioning from high to lower resolution, the SFR and gas surface density will be decreased by approximately the same factor. If  $N = 1$ , the lower resolution data will still lie on the same relation as the higher-resolution data, but at lower gas and SFR surface densities. In contrast, if  $N > 1$  ( $N < 1$ ), the lower resolution observations will be positively (negatively) offset from the higher resolution observations. This effect could contribute to our observed offset if  $N > 1$  because our data probe up to 3.2 kpc scales and the Bigiel et al. (2008) data has 750 pc resolution. We cannot provide a firm explanation for the offset between our data and the Bigiel et al. (2008) fit, but possible reasons for the offset include the use of different star formation tracers and resolutions,  $X_{\text{CO}}$  variation, and true SFE differences.

#### 4.1.3. Total Hydrogen Kennicutt-Schmidt Law

Figure 5 shows the relationship between the star formation rate surface density and the total hydrogen surface density. The vertical dashed line again shows the typical maximum H I density that is observed in most nearby galaxies. The Spearman rank correlation coefficient for our data and also the Bigiel et al. (2008) data is 0.8. This correlation is stronger than the correlation between SFR surface density and either atomic or molecular hydrogen surface density. In their study of star formation in the atomic-dominated regime, Schrubba et al. (2011) found that the rank correlation coefficient between SFR surface density and total hydrogen surface density is similar to or somewhat larger than the value for the correlation with the molecular hydrogen surface density. However, they noted that data can be correlated with a strong rank statistic even if the parameters are related by different functions in the atomic- and molecular-dominated regimes. As in the Schrubba et al. study, our stronger total hydrogen correlation is not likely related to fundamental physics.

The solid black line shows the Krumholz et al. (2009) model with  $0.4 Z_{\odot}$  metallicity. The model assumes a clumping factor,  $c$ , that is the inverse of the filling factor of  $\sim 100$  pc-sized atomic-molecular complexes in the beam. This value is not constrained well by data, so we assume the same value as Krumholz et al. (2009):  $c = 5$ . The magenta dot-dashed line shows the Kennicutt (1998) fit to a sample of normal and starburst galaxies, where the measurements are averages over the entire optical disk. The blue dotted line shows the Kennicutt et al. (2007) fit to regions in M51 that were studied at 520 pc resolution. Kennicutt et al. (2007) attribute the offset between the blue and magenta lines to dilution effects when the power-law index of the star formation law is not 1.0 (as discussed in Section 4.1.2).

#### 4.2. No Transition in SFE with Circular Velocity

In Section 1, we discussed that there could be a SFE transition in bulgeless disk galaxies at  $v_{\text{circ}} = 120 \text{ km s}^{-1}$ , depending on the star formation model assumed. In this section we show that there is no offset between the low- and high- $v_{\text{circ}}$  galaxies on the star formation law. In Sec-

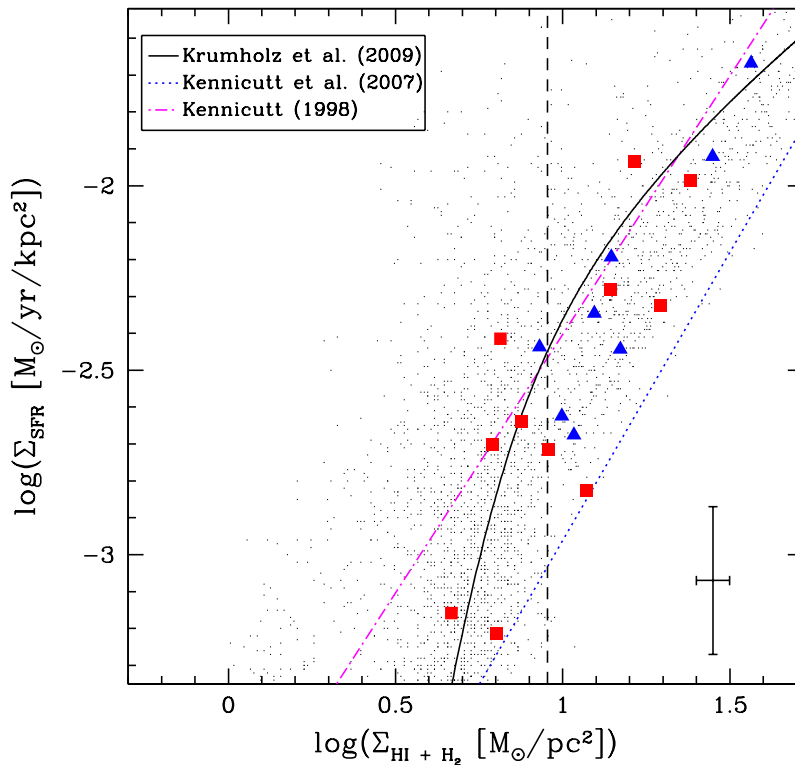


FIG. 5.— SFR surface density versus total hydrogen surface density. Symbols are as in Figure 3. The magenta dot-dashed line shows the Kennicutt (1998) fit to a sample of 61 normal spirals and 36 starburst galaxies, where the measurements are averages over the optical disk. The dotted line shows the Kennicutt et al. (2007) fit to M51 data at 520 pc resolution. The solid black line shows the Krumholz et al. (2009) model at  $0.4 Z_{\odot}$  metallicity.

tion 5, we interpret this result to discuss the relationship between SFE and the scale height of the cold ISM.

In Figures 3, 4, and 5, there is a slight trend for low- $v_{\text{circ}}$  galaxies to lie at lower surface densities compared to high- $v_{\text{circ}}$  galaxies, with average low- versus high- $v_{\text{circ}}$  surface densities as follows:  $\log(\Sigma_{\text{HI}}) = 0.9$  versus 1.0,  $\log(\Sigma_{\text{H}_2}) < 0.6$  versus  $= 0.9$ ,  $\log(\Sigma_{\text{HI}+\text{H}_2}) = 1.1$  versus 1.2, and  $\log(\Sigma_{\text{SFR}}) = -2.4$  versus  $-2.2$ . However, the differences are not significant; the Kolmogorov-Smirnov (K-S) test probabilities that the low- versus high- $v_{\text{circ}}$  galaxies are drawn from the same population in  $\Sigma_{\text{H}_2}$ ,  $\Sigma_{\text{HI}+\text{H}_2}$ , and  $\Sigma_{\text{SFR}}$  are 0.04, 0.2, and 0.2, respectively.

Figure 6 shows the distribution of SFE in the low- $v_{\text{circ}}$  (red solid) and high- $v_{\text{circ}}$  (blue dashed) galaxies. If the slope of the star formation law is not 1.0, a sample that follows the relation would have SFE that varies as a function of  $\Sigma_{\text{HI}+\text{H}_2}$ , which will tend to broaden the distributions. However, our low- and high- $v_{\text{circ}}$  objects have similar  $\Sigma_{\text{HI}+\text{H}_2}$  distributions, so this should not lead to spurious offsets between the samples. Furthermore, the  $\Sigma_{\text{HI}+\text{H}_2}$  range is not so great that it would hide any differences between the samples. We find no significant difference between the SFE distributions, with a K-S test probability of 0.8 that the low- and high- $v_{\text{circ}}$  galaxies are drawn from the same population.

We conclude that our sample of bulgeless disk galaxies does not show a strong transition in SFE at  $v_{\text{circ}} =$

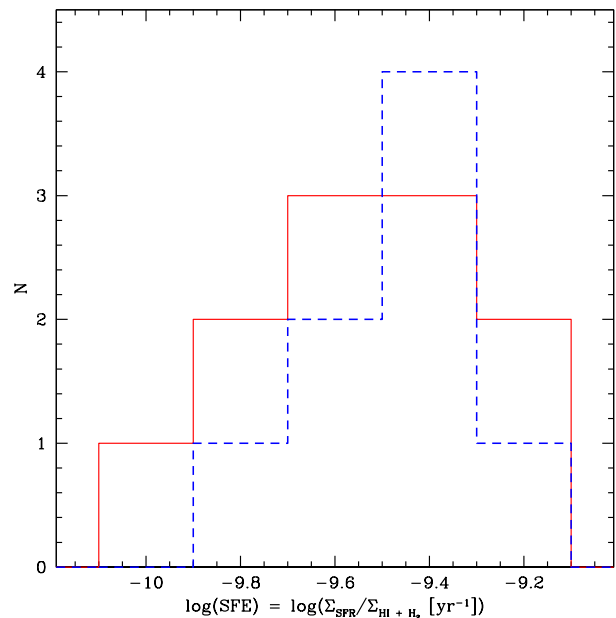


FIG. 6.— SFE histograms of the low- $v_{\text{circ}}$  (red solid) and high- $v_{\text{circ}}$  (blue dashed) samples. There is no significant difference between the distributions.

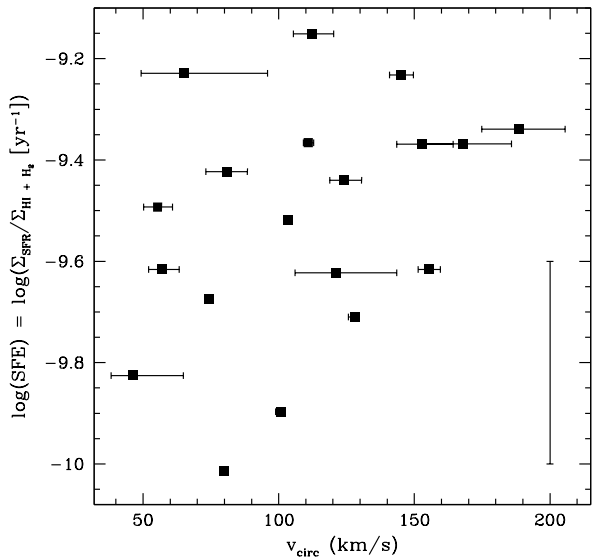


FIG. 7.— SFE versus circular velocity. There is no circular velocity at which a transition in SFE occurs.

$120 \text{ km s}^{-1}$ , where Dalcanton et al. (2004) concluded that there is a strong transition in dust scale height. In Figure 7 we show that there is no circular velocity at which there is a transition in SFE. Furthermore, there is no strong trend of SFE with circular velocity within the range we probe. Finally, we find no difference in the ratio of the molecular to atomic surface density between the low- and high- $v_{\text{circ}}$  galaxies (the K-S test probability that the samples are drawn from the same  $R_{\text{mol}}$  population is 0.4), nor do we find a transition in  $R_{\text{mol}}$  at any circular velocity (Figure 8).

#### 4.3. SFE Trends with Stability and Mid-plane Pressure

In this section, we address whether our sample shows a transition or trends in stability or mid-plane pressure, using the  $Q_{\text{gas}}$ ,  $Q_{\text{stars}}$ ,  $Q_{\text{gas+stars,min}}$ , and  $P_{\text{h}}$  values calculated in Section 3.4. Figure 9 shows the SFE versus  $Q_{\text{gas}}$  (left),  $Q_{\text{stars}}$  (middle), and  $Q_{\text{gas+stars,min}}$  (right). We find no unstable regions. The SFE generally decreases with larger, more stable  $Q$  values, although the correlation is not strong. For SFE versus  $Q_{\text{gas}}$ ,  $Q_{\text{stars}}$ , and  $Q_{\text{gas+stars,min}}$ , we find Spearman rank correlation coefficients of -0.2, -0.3, and -0.2, respectively. The sign of this correlation is as expected, but one might instead have expected a sharp decrease in SFE when  $Q$  rises above 1. These results are qualitatively similar to those in Leroy et al. (2008).

Dalcanton et al. (2004) concluded that galaxies with  $v_{\text{circ}} < 120 \text{ km s}^{-1}$  are generally stable while galaxies with  $v_{\text{circ}} > 120 \text{ km s}^{-1}$  are generally unstable, especially in the central ( $r < l_*$ ) regions. Contrary to these results, we see no evidence for a transition in stability at  $v_{\text{circ}} = 120 \text{ km s}^{-1}$ ; the K-S test probability that the low- and high- $v_{\text{circ}}$  galaxies are drawn from the same population of  $Q_{\text{gas}}$ ,  $Q_{\text{stars}}$ , and  $Q_{\text{gas+stars,min}}$  is 0.5, 0.2, and 0.8, respectively.

There are two principal differences between our

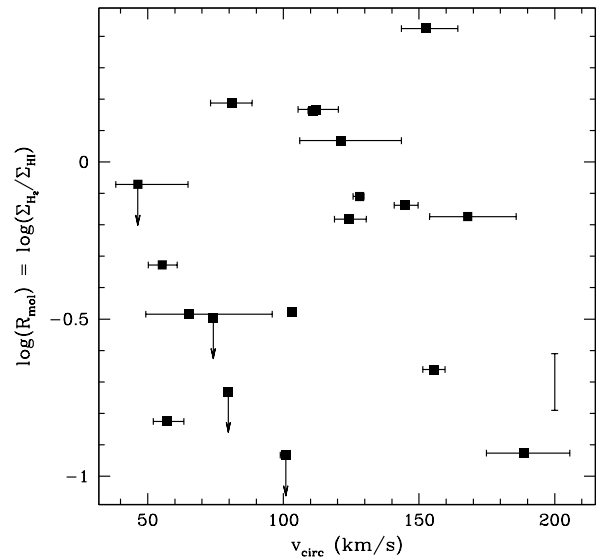


FIG. 8.— Ratio of the molecular to atomic gas surface density ( $R_{\text{mol}}$ ) versus circular velocity. There is no circular velocity at which a transition in  $R_{\text{mol}}$  occurs.

assumptions for the stability inputs and those in Dalcanton et al. (2004). First, we use a constant gas velocity dispersion and they used the quadrature sum of the velocity dispersion of atomic and molecular gas (10 and  $5 \text{ km s}^{-1}$ , respectively), weighted by the relative mass surface densities of the components. We use these assumptions and still find no difference in stability between the low- and high- $v_{\text{circ}}$  galaxies. Second, Dalcanton et al. (2004) estimated the molecular hydrogen surface densities for their sample from a scaling with circular velocities ( $\Sigma_{\text{H}_2} = (v_{\text{circ}}/47.1 \text{ km s}^{-1})^{2.49}$ ). This scaling relation was derived from a similar sample of galaxies with  $\Sigma_{\text{H}_2}$  values from Rownd & Young (1999) and  $v_{\text{circ}}$  estimated from single-dish H I data. Molecular hydrogen surface densities calculated using the scaling with  $v_{\text{circ}}$  are too large by a factor of six for our sample of high- $v_{\text{circ}}$  galaxies and too large by a factor of two for our sample of low- $v_{\text{circ}}$  galaxies. This discrepancy leads to smaller, less stable  $Q_{\text{gas}}$  and  $Q_{\text{gas+stars}}$  in the high- $v_{\text{circ}}$  galaxies relative to the low- $v_{\text{circ}}$  galaxies. However, even under these assumptions there is no significant difference between the low- and high- $v_{\text{circ}}$  galaxies in their  $Q$  values. Note that the difference in our molecular hydrogen surface densities compared to the values derived from the scaling with  $v_{\text{circ}}$  may also be related to resolution differences. Our  $\Sigma_{\text{H}_2}$  measurements are within the central  $21''$  while the Rownd & Young (1999) data have  $45''$  resolution and a similar distance distribution.

We test whether a stability transition occurs at any circular velocity in Figure 10, where we plot  $Q_{\text{gas+stars,min}}$  versus  $v_{\text{circ}}$ . There is no circular velocity below which the regions are stable and above which the regions are unstable. If any trend is present, it is that higher circular velocity objects are more stable.

We plot the SFE versus the mid-plane pressure in Figure 11. As seen in Leroy et al. (2008), we find an increase

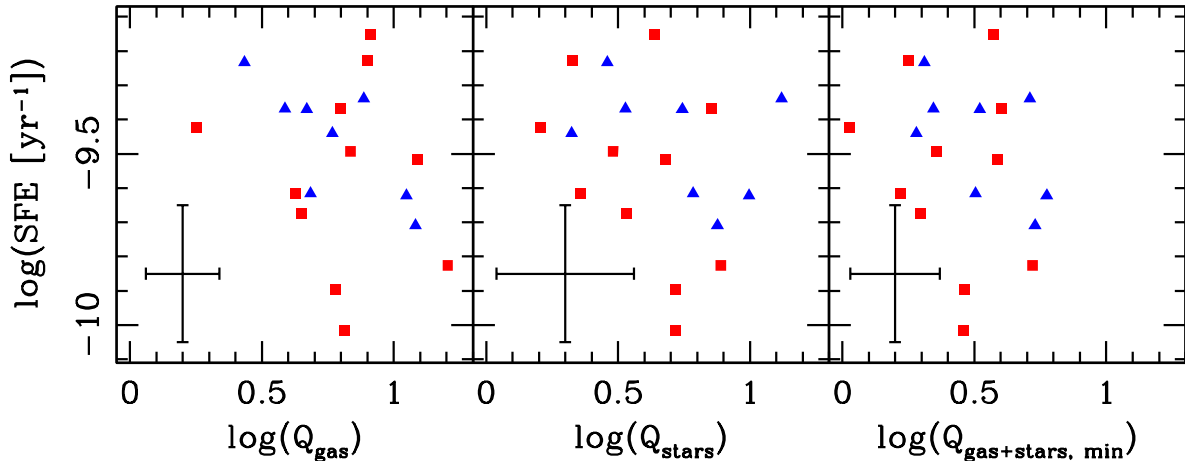


FIG. 9.— SFE ( $\Sigma_{\text{SFR}}/\Sigma_{\text{HI}+\text{H}_2}$ ) versus stability parameters  $Q_{\text{gas}}$  (left),  $Q_{\text{stars}}$  (middle), and  $Q_{\text{gas+stars, min}}$  (right). The symbols are as in Figure 3. Note that the condition for instability is  $Q \lesssim 1$ , so none of our galaxies are strictly unstable. We describe our derivation of the errorbar in Sections 3.2 and 3.4.

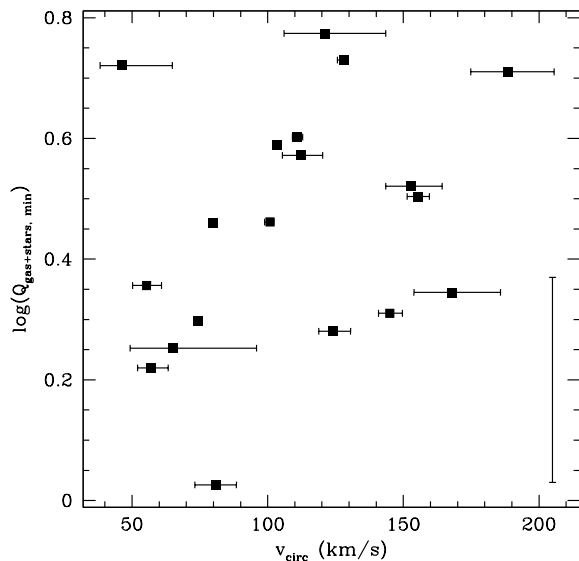


FIG. 10.— Stability parameter, including the gas and stellar contribution, versus circular velocity. There is no circular velocity at which a transition in stability occurs. We describe our derivation of the vertical errorbar in Section 3.4.

in SFE with increasing mid-plane pressure, but we do not probe high enough  $P_{\text{h}}$  values or have enough data points to sample the constant-SFE region of the diagram that is clear in Leroy et al. (2008). We find no difference between the low- and high- $v_{\text{circ}}$  galaxies in their  $P_{\text{h}}$  distributions, with a K-S test probability of 0.7 that they are drawn from the same population. Even focusing only on galaxies with the same  $\Sigma_{\text{HI}+\text{H}_2}$  (within the uncertainty in the parameter), the median pressure is the same in low- and high- $v_{\text{circ}}$  galaxies.

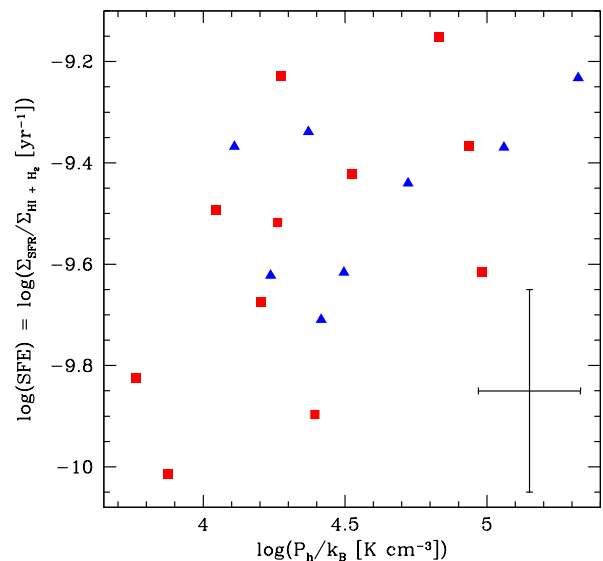


FIG. 11.— SFE versus mid-plane pressure. Symbols are as in Figure 3.

#### 4.4. Dependence of Star Formation on Metallicity

In this section, we use the oxygen abundance estimated from the stellar mass to study how star formation depends on metallicity and compare these results to recent theoretical work by Krumholz et al. (2009). At a given total gas surface density, the Krumholz et al. (2009) model predicts lower SFE at lower metallicity because  $\text{H}_2$  survival requires a higher column density as  $\text{H}_2$  self-shielding becomes more important than shielding by dust. This metallicity dependence distinguishes the model from other leading models, such as the model where mid-plane pressure determines where the ISM is molecular.

The left panel of Figure 12 shows the total hydrogen

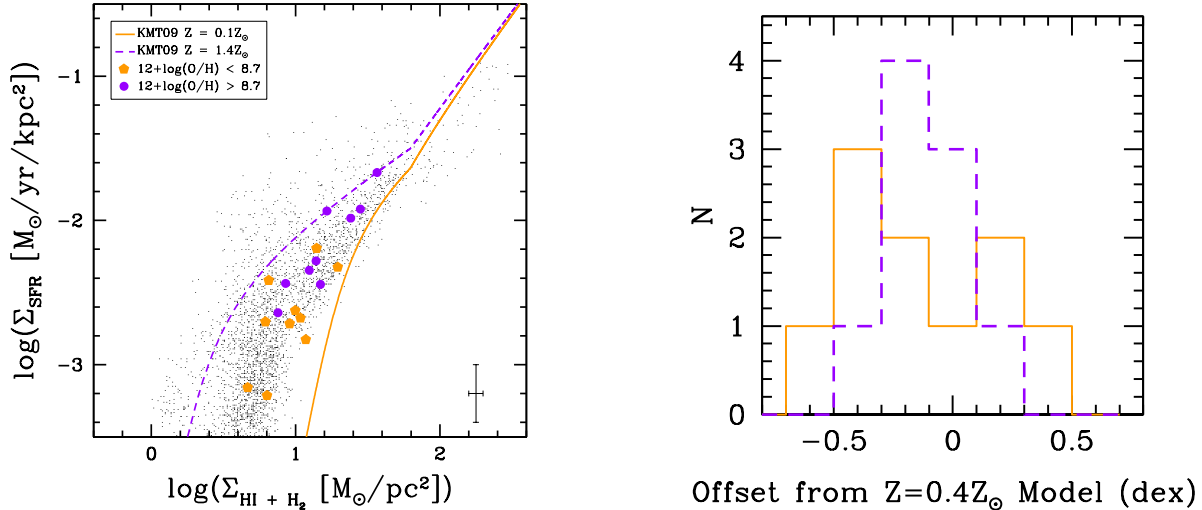


FIG. 12.— Left: SFR surface density versus total hydrogen surface density, as in Figure 5, but showing a larger range to demonstrate the model trends. The data are divided by oxygen abundance, where orange pentagons represent galaxies with  $12 + \log(O/H) < 8.7$  and purple circles represent galaxies with  $12 + \log(O/H) > 8.7$ . The lines show the Krumholz et al. (2009) model with a metallicity of  $0.1 Z_{\odot}$  (orange solid) and  $1.4 Z_{\odot}$  (purple dashed), which correspond to the lowest and highest metallicities in our sample. Right: Histograms of the offset of the data from the Krumholz et al. (2009) model with a metallicity of  $0.4 Z_{\odot}$ . The orange line represents the distribution of galaxies with  $12 + \log(O/H) < 8.7$  and the purple line represents the distribution of galaxies with  $12 + \log(O/H) > 8.7$ . There is no significant difference between the distributions.

star formation law, as plotted in Figure 5, except the galaxies are divided into low- $(O/H)$  and high- $(O/H)$ , with the division at  $12 + \log(O/H) = 8.7$ . The orange solid and purple dashed lines show the model of Krumholz et al. (2009) at  $0.1 Z_{\odot}$  and  $1.4 Z_{\odot}$ , respectively. These metallicities correspond to the extrema of our dataset, assuming  $Z/Z_{\odot} = (O/H)/(O/H)_{\odot}$  and  $12 + \log(O/H)_{\odot} = 8.86$  (Delahaye & Pinsonneault 2006). We see no evidence that the low- and high- $(O/H)$  galaxies cluster towards the low- and high- $Z$  models, respectively.

The right panel of Figure 12 shows the offset of our data from the  $0.4 Z_{\odot}$  Krumholz et al. (2009) model, which provides the best fit to our dataset as a whole (although note that we would expect the best fit to be the  $0.7 Z_{\odot}$  model, as that corresponds to the average  $(O/H)$  of our full sample). The orange solid and purple dashed lines show the distributions of our low- $(O/H)$  and high- $(O/H)$  galaxies, as divided in the left panel. If our data clearly followed the Krumholz et al. (2009) model, high- $(O/H)$  galaxies would be positively offset from the  $0.4 Z_{\odot}$  model and low- $(O/H)$  galaxies would be negatively offset. We find no significant difference between the offset of the low- versus high- $(O/H)$  galaxies (the K-S test probability that the samples are drawn from the same offset population is 0.14). A second order effect is that the offset from the  $0.4 Z_{\odot}$  model is expected to decrease with increasing  $\Sigma_{\text{HI}+\text{H}_2}$ . This may be related to the narrower offset distribution for the high- $(O/H)$  galaxies, which tend to have higher  $\Sigma_{\text{HI}+\text{H}_2}$ .

Figure 13 shows that there is a correlation between SFE and oxygen abundance in our data. For comparison, the line represents the Krumholz et al. (2009) model, where the SFE depends on metallicity,  $\Sigma_{\text{gas}}$ , and the filling factor. We have plotted the Krumholz et al. (2009) model with  $\log(\Sigma_{\text{HI}+\text{H}_2}) = 0.8$  (no He). This is a low

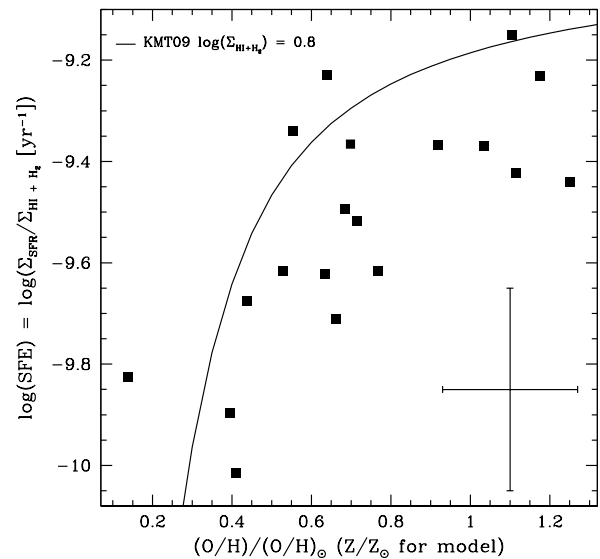


FIG. 13.— SFE versus oxygen abundance, scaled to the solar value. The solid line demonstrates the SFE trend with metallicity for the Krumholz et al. (2009) model at  $\log(\Sigma_{\text{HI}+\text{H}_2}) = 0.8$ .

$\Sigma_{\text{HI}+\text{H}_2}$  value compared to our data. Higher  $\Sigma_{\text{HI}+\text{H}_2}$  models reach constant SFE at lower metallicity. The mismatch between the average  $\Sigma_{\text{HI}+\text{H}_2}$  in the data and the best-fit  $\Sigma_{\text{HI}+\text{H}_2}$  used in the model is likely due to our assumptions for  $X_{\text{CO}}$  and the IMF in the data, our filling factor assumption in the model, and to uncertainties in the metallicity scale. For the latter, various strong-line metallicity methods return  $12 + \log(O/H)$  values

as disparate as 0.5 dex (Kewley & Ellison 2008), and it is unknown which calibration best aligns with the solar value. Therefore, the model line in Figure 13 only represents the expected trend of lower SFE at lower metallicity, at a given  $\Sigma_{\text{gas}}$ . At this level, the data do show the expected trend, with a Spearman correlation coefficient of 0.6. However, upon closer inspection, this agreement is mainly due to the fact that lower- $(O/H)$  galaxies tend to have lower  $\Sigma_{\text{HI}+\text{H}_2}$  (this is most obvious in Figure 12, although also note that the K-S test probability is 0.05 that the  $\Sigma_{\text{HI}+\text{H}_2}$  distributions of the low- and high- $(O/H)$  samples are drawn from the same population, which is not strong evidence for a difference). Because of their lower  $\Sigma_{\text{HI}+\text{H}_2}$  values, the low- $(O/H)$  galaxies are closer to the atomic-dominated regime of the star formation law where SFEs are lower. This is of course consistent with the Krumholz et al. (2009) model, but is not a discriminating test of the model because many other properties correlate with gas surface density (for examples, see Leroy et al. 2008). A sample with a range of directly-measured metallicities within a small range of gas surface density would provide a more discriminating test. In summary, we see no clear evidence to support the Krumholz et al. (2009) model, but our data are also not inconsistent with it.

## 5. DISCUSSION

In Section 4.2, we found that there is no transition in molecular fraction or SFE at any circular velocity probed by our sample. In Section 4.3, we found that all our galaxies are formally stable. While we did find a general trend of decreasing SFE with larger, more stable Q values, we found no sharp transition in stability at any circular velocity. Finally in Section 4.4, we found that SFE decreases at lower oxygen abundance, but the trend is not a particularly constraining test of the Krumholz et al. (2009) model. In this section, we first address our assumption that there is a transition in dust scale height at  $v_{\text{circ}} = 120 \text{ km s}^{-1}$ , rather than a transition in dust content. We then interpret our results to discuss the relationship between SFE and the scale height of the cold ISM. Finally, we comment on the scale of physical processes that affect star formation and discuss our results in the context of leading star formation models.

### 5.1. A Transition in Dust Scale Height versus Dust Content

In this section, we investigate the argument that the dust structure transition observed by Dalcanton et al. (2004) is due to a transition in dust scale height rather than due to a transition in the amount of dust present. Dalcanton et al. (2004) came to this conclusion because the dust structure transition occurs over a narrow range in circular velocity, where a large change in the DGR, and therefore dust content, is unexpected. All but one galaxy in our sample are detected at *Infrared Astronomical Satellite* 60 and  $100 \mu\text{m}$ , which indicates that there is at least some dust in the low- $v_{\text{circ}}$  galaxies. We estimated a DGR proxy as the ratio of the total infrared luminosity ( $L_{\text{TIR}}$ ), calculated with IRAS 25, 60, and  $100 \mu\text{m}$  data (Moshir et al. 1990) and the Dale & Helou (2002) relation, to the combined atomic and molecular hydrogen mass. We find no transition in this DGR proxy at  $v_{\text{circ}} = 120 \text{ km s}^{-1}$ , nor do we find any correlation be-

tween the DGR proxy and circular velocity.  $L_{\text{TIR}}$  is not necessarily proportional to the dust mass because the dust temperature may not be the same for all the galaxies; nevertheless, there is clearly a significant amount of dust in the low- $v_{\text{circ}}$  galaxies.

Two recent studies have found convincing evidence that low- $v_{\text{circ}}$  spirals have large dust scale heights. Seth et al. (2005) carried out a resolved stellar population study of six edge-on, late-type spirals with  $v_{\text{circ}} = 67 - 131 \text{ km s}^{-1}$  and found that the scale height of the young ( $\lesssim 10^8 \text{ yr}$ ) stellar population, which presumably formed from the cold ISM, is larger than in the Milky Way. MacLachlan et al. (2011) modeled the spectral energy distribution (SED) of three edge-on, low surface brightness galaxies with  $v_{\text{circ}} = 88 - 105 \text{ km s}^{-1}$  and found that a significant amount of dust must be present to account for the FIR (70 and  $160 \mu\text{m}$ ) emission, but the dust must have a large scale height such that it does not significantly obscure the optical emission. The authors concluded that the galaxies have dust scale heights greater than or equal to the stellar scale heights. This is in contrast to modeling studies of high surface brightness galaxies, which concluded that the dust scale height is about half the stellar scale height (e.g., Xilouris et al. 1999).

Hunter & Elmegreen (2006) provided an alternative explanation for the dust structure transition observed by Dalcanton et al. (2004). The authors studied a large sample of irregular galaxies and found that the average B-band surface brightness is smaller than in higher-mass spiral galaxies. Based on this result, they suggested that lower stellar surface density is the cause of the larger scale heights in low- $v_{\text{circ}}$  galaxies. They discussed that disk stability could correlate with the dust structure but not be the cause of the transition because the gas scale height ( $h_{\text{gas}} \propto \frac{\sigma_{\text{gas}}^2}{G\rho}$ , where  $\rho$  is the mass volume density of gas and stars; Blitz & Rosolowsky 2004) shares many of the same parameters with the stability parameter.

The authors discussed that dust opacity may also contribute to the observed difference in dust structure because of two effects. First, lower- $v_{\text{circ}}$  objects should have lower metallicity, and therefore lower dust content. Second, the scale length of a lower-mass galaxy is smaller and therefore a low- $v_{\text{circ}}$ , edge-on galaxy will have less depth from the edge to the center over which to accumulate dust column density compared to a high- $v_{\text{circ}}$  galaxy. Note that no scale height transition is needed in this interpretation. However, dust opacity is not likely the sole cause of the dust structure transition because of the reasons listed above. Hunter & Elmegreen (2006) suggested that the observed dust structure transition is likely due to a combination of stellar surface density and dust opacity. The authors agreed that a scale height transition does occur, so if this interpretation is correct, we can still constrain the effect of scale height differences on SFE.

In Sections 5.2 and 5.3, we assume that the dust scale heights in low- $v_{\text{circ}}$  galaxies are a factor of two larger than in high- $v_{\text{circ}}$  galaxies. Dalcanton et al. (2004) estimated this factor by examining the dust morphology in *Hubble Space Telescope* images of a couple edge-on, late-type galaxies. This factor is consistent with the SED modeling results of MacLachlan et al. (2011) and Xilouris et al. (1999) if the stellar scale height distribu-



tions of low- and high- $v_{\text{circ}}$  galaxies have significant overlap, which Dalcanton et al. (2004) found to be true (although there are low- $v_{\text{circ}}$  galaxies where the stellar scale height is about half the value in high- $v_{\text{circ}}$  galaxies, in which case the dust scale heights may be comparable).

### 5.2. The Relationship between SFE and Scale Height

In Section 4.2, we found no transition in SFE at  $v_{\text{circ}} = 120 \text{ km s}^{-1}$  or at any circular velocity probed by our sample. In this section, we interpret this result to discuss the relationship between SFE and the scale height of the cold ISM. For this discussion, we make a number of assumptions. First, we assume that our sample of bulgeless disk galaxies is similar to that of Dalcanton et al. (2004) in that galaxies with  $v_{\text{circ}} > 120 \text{ km s}^{-1}$  have narrow dust lanes while galaxies with  $v_{\text{circ}} < 120 \text{ km s}^{-1}$  have no obvious dust lanes. This is a reasonable assumption because it was our main consideration in choosing the sample, but because our galaxies are moderately inclined rather than edge-on, we are unable to directly measure the vertical dust structure. Second, as in Dalcanton et al. (2004), we assume that the dust scale heights in the low- $v_{\text{circ}}$  galaxies are larger than in the high- $v_{\text{circ}}$  galaxies (Section 5.1 addresses this assumption). Finally, we assume that the molecular gas and dust scale heights are comparable.

Dalcanton et al. (2004) suggested that there may be a SFE transition associated with the dust scale height transition at  $v_{\text{circ}} = 120 \text{ km s}^{-1}$ . The authors gave an example that assumes the true star formation law is a correlation between the volume density of gas ( $\rho_{\text{gas}}$ ) and the SFR volume density ( $\rho_{\text{SFR}}$ ):  $\rho_{\text{SFR}} \propto \rho_{\text{gas}}^N$ . The larger scale heights of low- $v_{\text{circ}}$  galaxies lead to lower gas volume densities. Depending on the index,  $N$ , a low- $v_{\text{circ}}$  galaxy with the same gas surface density as a high- $v_{\text{circ}}$  galaxy can have a lower SFR surface density and therefore a lower SFE. To consider this point, we first assume the same  $\Sigma_{\text{gas}}$  for a low- and high- $v_{\text{circ}}$  galaxy and the following relationships between the surface and volume density of gas and SFR:  $\Sigma_{\text{gas}} \propto \rho_{\text{gas}} h$ , and  $\Sigma_{\text{SFR}} \propto \rho_{\text{SFR}} h$ , where  $h$  is the scale height of the star forming gas and newly formed stars and the proportionality constant is the same for both relationships. We set  $\beta$  equal to the ratio of dust scale heights in low- $v_{\text{circ}}$  (lv) versus high- $v_{\text{circ}}$  (hv) galaxies:  $\beta = h_{\text{lv}}/h_{\text{hv}}$ . Dalcanton et al. (2004) very approximately estimated this ratio to be about two. Under these assumptions,  $\Sigma_{\text{SFR,hv}} = \beta^{N-1} \Sigma_{\text{SFR,lv}}$ , where  $\Sigma_{\text{SFR,hv}}$  and  $\Sigma_{\text{SFR,lv}}$  are the star formation rate surface densities of the low- and high- $v_{\text{circ}}$  galaxy with the same  $\Sigma_{\text{gas}}$ . Dalcanton et al. (2004) discussed the case where  $\beta = 2$  and  $N = 1.5$ , where we expect the high- $v_{\text{circ}}$  galaxy to have a  $\Sigma_{\text{SFR}}$  that is a factor of 1.4 larger than the low- $v_{\text{circ}}$  galaxy. Note that if  $N = 1$  there is no expected difference in star formation rate surface density.

In the star formation law plots of Figures 3, 4, and 5, we are sensitive to offsets in intercept between the low- and high- $v_{\text{circ}}$  samples that are greater than the uncertainty in the intercept, which is  $\sim 0.3 - 0.4$  dex, assuming an uncertainty in  $\Sigma_{\text{SFR}}$  of 0.2 dex and the number of galaxies in our low- and high- $v_{\text{circ}}$  samples. In the case discussed by Dalcanton et al. (2004), we expect the low- $v_{\text{circ}}$  galaxies to be offset to lower  $\Sigma_{\text{SFR}}$  by 0.15 dex. Therefore, we cannot exclude offsets at the level expected by Dalcanton et al. (2004).

The star formation law assumed above is not likely cor-

rect given that recent studies have found a strong molecular star formation law and no atomic gas star formation law. However, we can also determine the expected  $\Sigma_{\text{SFR}}$  offset if the molecular fraction is set by the mid-plane pressure and the molecular SFE is constant (see also Section 1). We assume the same  $\Sigma_{\text{HI+H}_2}$  for a low- and high- $v_{\text{circ}}$  galaxy,  $R_{\text{mol}} \propto P_{\text{h}}$ , and  $P_{\text{h}} \propto \rho_{\text{HI+H}_2} \sigma_{\text{gas}}^2$ , where  $\rho_{\text{HI+H}_2}$  is the total hydrogen volume density and the velocity dispersion of the gas is constant. In this scenario,  $\rho_{\text{HI+H}_2}$ ,  $P_{\text{h}}$ , and  $R_{\text{mol}}$  are lower by a factor of  $\beta$  in the low- $v_{\text{circ}}$  galaxy compared to the high- $v_{\text{circ}}$  galaxy. The expected offset in  $\Sigma_{\text{SFR}}$  depends on  $R_{\text{mol}}$ , which varies from 0.1 to 2.7 in our sample. If  $\beta = 2$  and  $R_{\text{mol}}$  of the high- $v_{\text{circ}}$  galaxy is 0.1 (2.7), we expect  $\Sigma_{\text{SFR}}$  to be lower by 0.3 dex (0.1 dex) in the low- $v_{\text{circ}}$  galaxy compared to the high- $v_{\text{circ}}$  galaxy. Given our uncertainties, this level of offset would also be difficult to detect. However, we can reject our assumption that  $P_{\text{h}}$  is lower by a factor of two in low- $v_{\text{circ}}$  galaxies. This is evident from Section 4.3, where we found no significant difference in the mid-plane pressure distributions of the low- and high- $v_{\text{circ}}$  galaxies, even when considering only objects with the same  $\Sigma_{\text{HI+H}_2}$ . Furthermore, we found no difference in the  $R_{\text{mol}}$  distributions of the low- versus high- $v_{\text{circ}}$  galaxies (Section 4.2).

The two scenarios explored above predict offsets in intercept between the low- and high- $v_{\text{circ}}$  samples that are less than the uncertainty. Therefore, we cannot clearly exclude these options. Nonetheless, our data show no evidence for a strong transition in SFE at any circular velocity. A simple interpretation that is consistent with our data is that low- $v_{\text{circ}}$  galaxies have a lower number of molecular clouds per unit volume compared to high- $v_{\text{circ}}$  galaxies at the same  $\Sigma_{\text{HI+H}_2}$ , but lower only by the ratio of the cold ISM scale heights in low- versus high- $v_{\text{circ}}$  galaxies. This results in the same total number of molecular clouds within the beam for a low- and high- $v_{\text{circ}}$  galaxy at the same  $\Sigma_{\text{HI+H}_2}$  and thus gives the same  $\Sigma_{\text{H}_2}$  and  $\Sigma_{\text{SFR}}$  (assuming the molecular clouds have the same density and that we average over evolutionary effects). Note that the above applies in the molecular-dominated regime. We have few data points below  $\Sigma_{\text{HI+H}_2} \sim 9 M_{\odot} \text{ pc}^{-2}$ , but expect that  $\Sigma_{\text{SFR}}$  can vary substantially for galaxies with the same  $\Sigma_{\text{HI+H}_2}$ , depending on the physical processes that affect the molecular fraction (e.g., those processes discussed in Krumholz et al. 2009 and Ostriker et al. 2010).

In conclusion, we interpret our result that there is no transition in SFE at any circular velocity as evidence that scale height differences at the level of about a factor of two do not significantly affect the molecular fraction or SFE in bulgeless disk galaxies. However, offsets in SFE below our uncertainty level are still possible.

### 5.3. Comparison to Star Formation Models

Dalcanton et al. (2004) very approximately estimated that the dust scale heights of low- $v_{\text{circ}}$  galaxies are about a factor of two larger than high- $v_{\text{circ}}$  galaxies. Assuming our sample has a similar range in scale height, our results indicate that these scale height differences, which lead to gas volume density differences also at the level of a factor of about two, do not lead to obvious differences in the SFE. Our results favor star formation models where small-scale physical processes are more important than

processes that act on larger scales, of order the dust and cold gas scale height (10s to 100 pc). Based on their comparison to many star formation models without an obvious favorite, Leroy et al. (2008) discussed that physics below their resolution of 750 pc is likely most important for determining the SFE. We contribute with a further constraint that the SFE is likely affected primarily by processes that act on scales smaller than the cold gas and dust scale height.

We cannot exclude all star formation models that include large-scale physics because there are processes that may affect star formation but are neither affected by nor affect the scale height. For example, our sample has no power to constrain the effects of large-scale radial processes, like shear (see, e.g., Hunter et al. 1998), on star formation. In addition, star formation may be affected by environmental properties that depend on the gas volume density but also depend on other variables that counteract a variable volume density. For example, the pressure in the ISM is related to the gas volume density and velocity dispersion:  $P \propto \rho_{\text{gas}} \sigma_{\text{gas}}^2$ . While we expect the volume density to be lower in low- $v_{\text{circ}}$  galaxies, the velocity dispersion may be larger. With the right combination of  $\rho_{\text{gas}}$  and  $\sigma_{\text{gas}}$ , there could be no difference in pressure between low- and high- $v_{\text{circ}}$  galaxies. While the latter argument illustrates our limitations, we note that there is currently no strong observational reason to assume different gas velocity dispersions between the low- and high- $v_{\text{circ}}$  galaxies. Tamburro et al. (2009) found some variation in the central H I velocity dispersion in eleven galaxies ranging from early-type spirals to irregulars, but more observations are needed.

Would leading star formation models have predicted a difference in SFE in galaxies with scale heights that differ by about a factor of two? In the Krumholz et al. (2009) model,  $\Sigma_{\text{SFR}}$  is a function of metallicity,  $\Sigma_{\text{gas}}$ , and the beam filling factor of  $\sim 100$  pc-sized atomic-molecular complexes. There is no direct dependence on the scale height, so we would not expect a transition in SFE unless there is a transition in the metallicity or filling factor with scale height. We find no transition in oxygen abundance at any circular velocity in our data, but there should be a correlation between these two properties given the mass-metallicity relation (e.g., Tremonti et al. 2004), which we also do not see. The filling factor of star-forming complexes is not well constrained, although there is no *a priori* reason to suppose that it would be different in low-versus high- $v_{\text{circ}}$  objects. Krumholz et al. (2009) do not predict a difference in SFE in galaxies with different scale heights and the fact that we did not find a transition in SFE at  $v_{\text{circ}} = 120 \text{ km s}^{-1}$  is not a strong constraint on this model.

In the model where the mid-plane pressure sets the molecular fraction and the molecular SFE is constant, the pressure is proportional to the gas volume density, which we expect to vary between the low- and high- $v_{\text{circ}}$  galaxies. If the gas velocity dispersion is fixed, we would expect the low- $v_{\text{circ}}$  galaxies to have lower molecular to atomic surface density ratios and lower SFEs relative to the high- $v_{\text{circ}}$  galaxies. However, we found no difference between the mid-plane pressure, molecular to atomic surface density ratio, or SFE distributions of the low- and high- $v_{\text{circ}}$  galaxies. If our assumptions are cor-

rect, our result is inconsistent with this model. However, the offset in SFE expected for galaxies with cold gas scale heights that differ by about a factor of two may be less than our SFE uncertainties. Furthermore, the Ostriker et al. (2010) model relates the molecular fraction (or in their terms, the fraction of gas in gravitationally bound complexes) to the pressure of the diffuse component of the ISM. We have a constraint only on the scale height and volume density of the cold component of the ISM; therefore the Ostriker et al. (2010) model may not predict molecular fraction and SFE differences in our sample. In general, our results are somewhat more consistent with local models of star formation, like the Krumholz et al. (2009) model, but we do not find conclusive evidence for or against either the Krumholz et al. (2009) or Ostriker et al. (2010) model.

One final matter to address is whether central measurements are sufficient to determine if there is a transition in molecular fraction, SFE, and/or stability at the dust structure transition of  $v_{\text{circ}} = 120 \text{ km s}^{-1}$ . One might question the use of central measurements because dust structure, SFE, and stability may be affected by the higher gas and stellar densities and shorter dynamical times characteristic of these regions. The only approach that will fully address this concern is to obtain off-center measurements of the above properties. Our single-beam CO data currently limit us from carrying out this analysis. Meanwhile, there is some evidence that our central pointings are sufficient to address these questions. First, our measurements trace a significant fraction of the disk: the  $21''$  aperture probes physical scales of  $0.7 - 3.2$  kpc, which is similar to the disk scale lengths of our sample ( $0.7 - 3.4$  kpc). Second, the central regions of bulgeless galaxies are more morphologically and kinematically similar to the outskirts than in a galaxy with a bulge. Finally, we expect a galaxy to be less stable against gravitational collapse in the center compared to the outer disk because the gas and stellar surface densities are larger. However, we find that both the low- and high- $v_{\text{circ}}$  galaxies are stable. This suggests that there would also not be a stability transition at  $v_{\text{circ}} = 120 \text{ km s}^{-1}$  in off-center measurements because both the low- and high- $v_{\text{circ}}$  galaxies would be more stable.

## 6. SUMMARY

We have presented a study of star formation in twenty moderately-inclined, bulgeless disk galaxies. We found no transition in star formation efficiency ( $\Sigma_{\text{SFR}}/\Sigma_{\text{HI+H}_2}$ ) or disk stability at  $v_{\text{circ}} = 120 \text{ km s}^{-1}$ . This circular velocity was previously found to be associated with a transition in the vertical dust structure of edge-on, bulgeless disk galaxies that is most likely due to a transition in the scale height of the cold ISM. We also found no transition in star formation efficiency or disk stability at any circular velocity probed by our sample. Our results demonstrate that the scale height of the cold ISM does not play a major role in setting the molecular fraction or the star formation efficiency. We also found decreasing star formation efficiency with lower oxygen abundance, which we estimated from the stellar mass. This result is consistent with the recent Krumholz et al. (2009) model, but a sample with a large range of metallicities within a small range of gas surface density would provide a more constraining test of the model. In general, our results

are most consistent with local models of star formation that include physical processes that act on smaller scales than the dust and cold gas scale height (10s to 100 pc).

We thank Frank Bigiel for providing us with his data. We are also grateful to Todd A. Thompson for helpful comments and discussion, Richard W. Pogge for supplying the narrowband filters used in the H $\alpha$  observations, Roberto J. Assef, David W. Atlee, and Katharine J. Schlesinger for obtaining some of the H $\alpha$  observations, and the referee for comments that improved this work. L.C.W. gratefully acknowledges support from an NSF Graduate Research Fellowship and an Ohio State University Distinguished University Fellowship. PM is grateful for support from the NSF via award AST-

0705170. U.L. acknowledges financial support from the research projects AYA2007-67625-C02-02 and AYA2011-24728 from the Spanish Ministerio de Ciencia y Educación and from the Junta de Andalucía. This work is based in part on observations made with the Spitzer Space Telescope, which is operated by the Jet Propulsion Laboratory, California Institute of Technology under a contract with NASA. Support for this work was provided by NASA through an award issued by JPL/Caltech. This publication makes use of data products from the Two Micron All Sky Survey, which is a joint project of the University of Massachusetts and the Infrared Processing and Analysis Center/California Institute of Technology, funded by the National Aeronautics and Space Administration and the National Science Foundation.

## REFERENCES

- Bell, E. F., & de Jong, R. S. 2001, *ApJ*, 550, 212
- Bertin, E. 2006, *Astronomical Data Analysis Software and Systems XV*, 351, 112
- Bertin, E., & Arnouts, S. 1996, *A&AS*, 117, 393
- Bertin, E., Mellier, Y., Radovich, M., Missonnier, G., Didelon, P., & Morin, B. 2002, *Astronomical Data Analysis Software and Systems XI*, 281, 22
- Bigiel, F., Leroy, A., Walter, F., Brinks, E., de Blok, W. J. G., Madore, B., & Thornley, M. D. 2008, *AJ*, 136, 2846
- Blanc, G. A., Heiderman, A., Gebhardt, K., Evans, N. J., II, & Adams, J. 2009, *ApJ*, 704, 842
- Blitz, L., & Rosolowsky, E. 2004, *ApJ*, 612, L29
- Blitz, L., & Rosolowsky, E. 2006, *ApJ*, 650, 933
- Böker, T., Lisenfeld, U., & Schinnerer, E. 2003, *A&A*, 406, 87
- Bolatto, A. D., Leroy, A. K., Rosolowsky, E., Walter, F., & Blitz, L. 2008, *ApJ*, 686, 948
- Bolatto, A. D., Leroy, A. K., Jameson, K., et al. 2011, *ApJ*, 741, 12
- Brook, C. B., et al. 2011, *MNRAS*, 595
- Bruzual, G., & Charlot, S. 2003, *MNRAS*, 344, 1000
- Calzetti, D., et al. 2007, *ApJ*, 666, 870
- Conroy, C., Gunn, J. E., & White, M. 2009, *ApJ*, 699, 486
- Dalcanton, J. J., Yoachim, P., & Bernstein, R. A. 2004, *ApJ*, 608, 189
- Dale, D. A., et al. 2009, *ApJ*, 703, 517
- Dale, D. A., & Helou, G. 2002, *ApJ*, 576, 159
- Delahaye, F., & Pinsonneault, M. H. 2006, *ApJ*, 649, 529
- de Vaucouleurs, G., de Vaucouleurs, A., Corwin, H. G., Jr., Buta, R. J., Paturel, G., & Fouque, P. 1991, *Third Reference Catalogue of Bright Galaxies* (New York: Springer)
- Doyle, M. T., et al. 2005, *MNRAS*, 361, 34
- Draine, B. T., et al. 2007, *ApJ*, 663, 866
- Elmegreen, B. G. 1989, *ApJ*, 338, 178
- Elmegreen, B. G. 1993, *ApJ*, 411, 170
- Epinat, B., Amram, P., & Marcelin, M. 2008, *MNRAS*, 390, 466
- Fukui, Y., & Kawamura, A. 2010, *ARA&A*, 48, 547
- Helou, G., et al. 2004, *ApJS*, 154, 253
- Hopkins, P. F., Hernquist, L., Cox, T. J., Younger, J. D., & Besla, G. 2008, *ApJ*, 688, 757
- Hora, J. L., et al. 2004, *Proc. SPIE*, 5487, 77
- Hunter, D. A., Elmegreen, B. G., & Baker, A. L. 1998, *ApJ*, 493, 595
- Hunter, D. A., & Elmegreen, B. G. 2006, *ApJS*, 162, 49
- James, P. A., Shane, N. S., Beckman, J. E., et al. 2004, *A&A*, 414, 23
- Jarrett, T. H., Chester, T., Cutri, R., Schneider, S. E., & Huchra, J. P. 2003, *AJ*, 125, 525
- Jedrzejewski, R. I. 1987, *MNRAS*, 226, 747
- Kautsch, S. J., Grebel, E. K., Barazza, F. D., & Gallagher, J. S., III 2006, *A&A*, 445, 765
- Kennicutt, R. C., Jr. 1983, *ApJ*, 272, 54
- Kennicutt, R. C., Jr. 1998, *ApJ*, 498, 541
- Kennicutt, R. C., Jr., et al. 2007, *ApJ*, 671, 333
- Kennicutt, R. C., et al. 2009, *ApJ*, 703, 1672
- Kewley, L. J., & Ellison, S. L. 2008, *ApJ*, 681, 1183
- Koopmann, R. A., Kenney, J. D. P., & Young, J. 2001, *ApJS*, 135, 125
- Kormendy, J., Drory, N., Bender, R., & Cornell, M. E. 2010, *ApJ*, 723, 54
- Kormendy, J., & Kennicutt, R. C., Jr. 2004, *ARA&A*, 42, 603
- Kregel, M., van der Kruit, P. C., & de Grijs, R. 2002, *MNRAS*, 334, 646
- Kroupa, P. 2001, *MNRAS*, 322, 231
- Krumholz, M. R., McKee, C. F., & Tumlinson, J. 2009, *ApJ*, 699, 850
- Lee, H., Skillman, E. D., Cannon, J. M., Jackson, D. C., Gehrz, R. D., Polomski, E. F., & Woodward, C. E. 2006, *ApJ*, 647, 970
- Leger, A., & Puget, J. L. 1984, *A&A*, 137, L5
- Leroy, A. K., Walter, F., Brinks, E., Bigiel, F., de Blok, W. J. G., Madore, B., & Thornley, M. D. 2008, *AJ*, 136, 2782
- Leroy, A. K., Bolatto, A., Gordon, K., et al. 2011, *ApJ*, 737, 12
- Liu, G., Koda, J., Calzetti, D., Fukuhara, M., & Momose, R. 2011, *ApJ*, 735, 63
- MacLachlan, J. M., Matthews, L. D., Wood, K., & Gallagher, J. S. 2011, *ApJ*, 741, 6
- Matthews, L. D., Gao, Y., Uson, J. M., & Combes, F. 2005, *AJ*, 129, 1849
- Moshir, M., & et al. 1990, *IRAS Faint Source Catalogue*, version 2.0 (1990)
- Mould, J. R., et al. 2000, *ApJ*, 529, 786
- Moustakas, J., & Kennicutt, R. C., Jr. 2006, *ApJS*, 164, 81
- O'Donnell, J. E. 1994, *ApJ*, 422, 158
- Oh, S.-H., de Blok, W. J. G., Walter, F., Brinks, E., & Kennicutt, R. C. 2008, *AJ*, 136, 2761
- Ostriker, E. C., McKee, C. F., & Leroy, A. K. 2010, *ApJ*, 721, 975
- Peeters, E., Spoon, H. W. W., & Tielens, A. G. G. M. 2004, *ApJ*, 613, 986
- Peng, C. Y., Ho, L. C., Impey, C. D., & Rix, H.-W. 2002, *AJ*, 124, 266
- Press, W. H., Teukolsky, S. A., Vetterling, W. T., & Flannery, B. P. 1992, *Numerical Recipes in C. The Art of Scientific Computing* (2nd ed.; Cambridge: Cambridge Univ. Press), 274
- Rafikov, R. R. 2001, *MNRAS*, 323, 445
- Rahman, N., et al. 2011, *ApJ*, 730, 72
- Reach, W. T., et al. 2005, *PASP*, 117, 978
- Robertson, B., Bullock, J. S., Cox, T. J., Di Matteo, T., Hernquist, L., Springel, V., & Yoshida, N. 2006, *ApJ*, 645, 986
- Romeo, A. B., & Wiegert, J. 2011, *MNRAS*, 416, 1191
- Rownd, B. K., & Young, J. S. 1999, *AJ*, 118, 670
- Scannapieco, C., White, S. D. M., Springel, V., & Tissera, P. B. 2011, *MNRAS*, 417, 154
- Schlegel, D. J., Finkbeiner, D. P., & Davis, M. 1998, *ApJ*, 500, 525
- Schmidt, M. 1959, *ApJ*, 129, 243
- Schruba, A., Leroy, A. K., Walter, F., Sandstrom, K., & Rosolowsky, E. 2010, *ApJ*, 722, 1699
- Schruba, A., et al. 2011, *AJ*, 142, 37
- Sellgren, K. 1984, *ApJ*, 277, 623
- Seth, A. C., Dalcanton, J. J., & de Jong, R. S. 2005, *AJ*, 130, 1574
- Shapiro, K. L., Gerssen, J., & van der Marel, R. P. 2003, *AJ*, 126, 2707
- Smith, J. D. T., et al. 2007, *ApJ*, 656, 770

- Swaters, R. A. 1999, Ph.D. Thesis
- Tamburro, D., Rix, H.-W., Leroy, A. K., Mac Low, M.-M., Walter, F., Kennicutt, R. C., Brinks, E., & de Blok, W. J. G. 2009, *AJ*, 137, 4424
- Toomre, A. 1964, *ApJ*, 139, 1217
- Tremonti, C. A., et al. 2004, *ApJ*, 613, 898
- Tully, R. B. 1988, Cambridge and New York, Cambridge University Press, 1988, 221 p.,
- Tully, R. B., Shaya, E. J., Karachentsev, I. D., Courtois, H. M., Kocevski, D. D., Rizzi, L., & Peel, A. 2008, *ApJ*, 676, 184
- van der Kruit, P. C., & Searle, L. 1981, *A&A*, 95, 105
- van der Kruit, P. C. 1988, *A&A*, 192, 117
- Watson, L. C., Schinnerer, E., Martini, P., Böker, T., & Lisensfeld, U. 2011, *ApJS*, 194, 36 (Paper I)
- Wong, T., & Blitz, L. 2002, *ApJ*, 569, 157
- Xilouris, E. M., Byun, Y. I., Kylafis, N. D., Paleologou, E. V., & Papamastorakis, J. 1999, *A&A*, 344, 868
- Yang, C.-C., Gruendl, R. A., Chu, Y.-H., Mac Low, M.-M., & Fukui, Y. 2007, *ApJ*, 671, 374
- Yim, K., Wong, T., Howk, J. C., & van der Hulst, J. M. 2011, *AJ*, 141, 48
- Zhu, Y.-N., Wu, H., Cao, C., & Li, H.-N. 2008, *ApJ*, 686, 155

TABLE 1  
GENERAL GALAXY PROPERTIES

Source	RA	DEC	D	$D_{25}$	$B$	$M_B$	Type	$V_{\text{sys}}$	$v_{\text{circ}}$	PA	$i$	$W_{20}$
(1)	(hh:mm:ss.s)	(dd:mm:ss)	(Mpc)	(arcsec)	(mag)	(mag)	(8)	( $\text{km s}^{-1}$ )	( $\text{km s}^{-1}$ )	( $^{\circ}$ )	( $^{\circ}$ )	( $\text{km s}^{-1}$ )
NGC 0337	00:59:50.0	-07:34:41	20.7 [T88]	173	11.44	-20.14	7.0	$1646 \pm 2$	$145^{+5}_{-4.6}$	$118 \pm 5$	$44 \pm 2$	261
PGC 3853	01:05:04.8	-06:12:46	11.4 [T08]	250	11.98	-18.30	7.0	$1094.7 \pm 0.4$	$128.1^{+12.6}_{-7}$	$105.3 \pm 0.2$	$41.4 \pm 1.1$	192
PGC 6667	01:49:10.3	-10:03:45	24.6 [T88]	173	12.92	-19.03	6.7	$1989.2 \pm 0.6$	$155^{+4}_{-4.4}$	$122.9 \pm 1.8$	$34.0 \pm 1.1$	198
ESO 544-G030	02:14:57.2	-20:12:40	13.9 [T08]	123	13.25	-17.47	7.7	$1608.4 \pm 1.0$	$100.9^{+12.4}_{-2}$	$107.6 \pm 1.1$	$48.5 \pm 1.2$	146
UGC 1862	02:24:24.8	-02:09:41	22.3 [T08]	99.6	13.47	-18.27	7.0	$1382.9 \pm 0.4$	$55^{+6}_{-5}$	$21.7 \pm 1.7$	$43 \pm 4$	125
ESO 418-G008	03:31:30.8	-30:12:46	23.6 [T08]	70.5	13.65	-18.21	8.0	$1195.4 \pm 0.3$	$74.1^{+0.6}_{-0.6}$	$317.9 \pm 1.1$	$55.6 \pm 1.4$	140
ESO 555-G027	06:03:36.6	-20:39:17	24.3 [T88]	138	13.18	-18.75	7.0	$1978.7 \pm 0.4$	$190^{+40}_{-2}$	$221.5 \pm 0.3$	$21 \pm 4$	162
NGC 2805	09:20:20.4	+64:06:12	28.0 [T88]	379	11.17	-21.07	7.0	$1732.6 \pm 0.6$	$81^{+20}_{-8}$	$300 \pm 3$	$38 \pm 4$	120
ESO 501-G023	10:35:23.6	-24:45:21	7.01 [T08]	208	12.86	-16.37	8.0	$1046.8 \pm 0.7$	$46^{+18}_{-8}$	$224 \pm 2$	$37 \pm 12$	83
UGC 6446	11:26:40.6	+53:44:58	18.0 [T08]	213	13.30	-17.98	7.0	$645.5 \pm 0.6$	$79.7^{+1.3}_{-0.8}$	$189.4 \pm 0.5$	$52.5 \pm 1.9$	150
NGC 3794	11:40:54.8	+56:12:10	19.2 [T08]	134	13.23	-18.19	6.5	$1384.9 \pm 0.7$	$103.3^{+1.1}_{-1.0}$	$123.1 \pm 1.1$	$54.8 \pm 1.3$	182
NGC 3906	11:49:40.2	+48:25:30	18.3 [...]	112	13.50	-17.81	7.0	$959.44 \pm 0.7$	$65^{+30}_{-16}$	$180 \pm 20$	$16 \pm 5$	49
UGC 6930	11:57:17.2	+49:17:08	17.0 [T88]	262	12.38	-18.77	7.0	$776.7 \pm 0.7$	$121^{+20}_{-15}$	$39.5 \pm 0.5$	$25 \pm 4$	140
NGC 4519	12:33:30.5	+08:39:16	19.6 [T08]	190	12.15	-19.31	7.0	$1218.1 \pm 1.0$	$112^{+8}_{-7}$	$355 \pm 2$	$42 \pm 3$	218
NGC 4561	12:36:08.6	+19:19:26	12.3 [T88]	90.8	12.82	-17.63	8.0	$1402.2 \pm 0.9$	$57^{+6}_{-5}$	$227 \pm 8$	$34 \pm 4$	171
NGC 4713	12:49:58.1	+05:18:39	14.9 [T08]	162	11.85	-19.02	7.0	$654.5 \pm 0.5$	$110.9^{+2}_{-1.8}$	$274.0 \pm 0.6$	$45.2 \pm 1.2$	176
NGC 4942	13:04:19.2	-07:39:00	28.5 [T88]	112	13.27	-19.00	7.0	$1741 \pm 2$	$124^{+6}_{-5}$	$137.3 \pm 0.8$	$37 \pm 2$	177
NGC 5964	15:37:36.3	+05:58:28	24.7 [T88]	250	12.28	-19.68	7.0	$1447.1 \pm 1.2$	$168^{+18}_{-14}$	$136.7 \pm 1.2$	$32 \pm 3$	208
NGC 6509	17:59:24.9	+06:17:12	28.2 [T88]	95.1	12.12	-20.13	7.0	$1811.0 \pm 0.4$	$153^{+12}_{-9}$	$280.8 \pm 1.1$	$41 \pm 4$	266
IC 1291	18:33:51.5	+49:16:45	31.5 [T88]	109	13.28	-19.21	8.0	$1951.0 \pm 1.1$	$189^{+17}_{-14}$	$131 \pm 2$	$28 \pm 3$	209

NOTE. — Column 1: Object name; Column 2 and 3: Right ascension and declination (J2000.0) from de Vaucouleurs et al. (1991); Column 4: Distance and distance reference. Distances are derived using the Tully-Fisher relation, except for NGC 3906. T08: Tully et al. (2008), T88: Tully (1988), and the NGC 3906 distance is from the de Vaucouleurs et al. (1991) heliocentric velocity, corrected for Virgo infall using Mould et al. (2000) and using  $H_0 = 71 \text{ km s}^{-1} \text{ Mpc}^{-1}$ . Column 5: Major isophotal diameter at 25 mag arcsec $^{-2}$  in the B band, from de Vaucouleurs et al. (1991). Column 6: Apparent blue magnitude, corrected for Galactic and internal extinction and redshift. Values are from de Vaucouleurs et al. (1991), except for NGC 4942 and PGC 6667, which are from Doyle et al. (2005) and are only corrected for Galactic extinction. Column 7: Absolute blue magnitude, calculated from the apparent magnitude in Column 6 and the distance in Column 4. Column 8: Morphological type from de Vaucouleurs et al. (1991). Column 9: Systemic velocity, corrected to the heliocentric reference frame. Column 10: Circular velocity. Columns 9 and 10 were derived from the VLA H I rotation curve analysis in Paper I. Column 11: Position angle of the major axis (degrees N to E to receding side). Column 12: Inclination. Columns 11 and 12 were derived from a combination of the rotation curve analyses on the H I data and ellipse fits of the IRAC 3.6  $\mu\text{m}$  data. Columns 9-12 were originally presented in Table 6 of Paper I. Column 13: Width of the HI line at 20% of the peak flux density, corrected for the spectral resolution but not turbulent broadening. The uncertainty in  $W_{20}$  is  $5 \text{ km s}^{-1}$  for all objects except UGC 6446 and NGC 3906, where the uncertainty is  $3 \text{ km s}^{-1}$  and  $10 \text{ km s}^{-1}$ , respectively. Column 13 was originally presented in Table 4 of Paper I.

TABLE 2  
MEASURED AND LITERATURE PROPERTIES

Source	RA	DEC	$F_{\text{H}\alpha}$	$F_{\text{PAH}}$	$\langle I_{\text{HI}} \rangle$	$B_{\text{maj}}$	$B_{\text{min}}$	$I_{\text{CO}}$	$F_{4.5}^{21''}$	$F_{4.5}^{D25}$	$J$	$K_s$
(1)	(hh:mm:ss.s)	(dd:mm:ss)	( $10^{-14}$ erg s $^{-1}$ cm $^{-2}$ )	(mJy)	(Jy beam $^{-1}$ km s $^{-1}$ )	(arcsec)	(arcsec)	(K km s $^{-1}$ )	(mJy)	(mJy)	(mag)	(mag)
	(2)	(3)	(4)	(5)	(6)	(7)	(8)	(9)	(10)	(11)	(12)	(13)
NGC 0337	00:59:49.9	-07:34:44	10.2 ± 0.05	73 ± 8	1.28 ± 0.17	25.77	15.06	4.7 ± 0.3	11.7 ± 1.2	64 ± 6	9.876 ± 0.025	9.059 ± 0.045
PGC 3853	01:05:04.9	-06:12:45	0.98 ± 0.04	6.9 ± 0.8	0.36 ± 0.05	25.33	15.47	1.39 ± 0.18	3.4 ± 0.3	44 ± 4	10.031 ± 0.037	9.280 ± 0.080
PGC 6667	01:49:10.3	-10:03:40	2.37 ± 0.02	8.5 ± 0.9	0.90 ± 0.12	26.00	21.00	0.71 ± 0.13	2.4 ± 0.2	15.2 ± 1.5	11.678 ± 0.037	10.951 ± 0.080
ESO 544-G030	02:14:56.8	-20:12:44	0.85 ± 0.02	5.3 ± 0.6	0.59 ± 0.08	27.78	12.01	< 0.4	2.5 ± 0.3	12.8 ± 1.3	...	...
UGC 1862	02:24:24.8	-02:09:44	1.97 ± 0.02	4.2 ± 0.5	0.24 ± 0.03	23.97	15.32	0.60 ± 0.10	2.2 ± 0.2	12.4 ± 1.2	11.927 ± 0.023	11.177 ± 0.054
ESO 418-G008	03:31:30.7	-30:12:48	1.84 ± 0.03	6.7 ± 0.8	0.92 ± 0.12	32.00	21.00	< 0.9	2.7 ± 0.3	6.7 ± 0.7	12.752 ± 0.049	12.169 ± 0.126
ESO 555-G027	06:03:36.8	-20:39:15	1.42 ± 0.05	9.3 ± 1.0	0.44 ± 0.06	29.00	21.00	...	2.4 ± 0.2	16.1 ± 1.6	11.984 ± 0.045	11.271 ± 0.103
NGC 2805	09:20:20.3	+64:06:11	2.53 ± 0.017	15.5 ± 1.7	0.34 ± 0.04	21.00	21.00	2.34 ± 0.10	4.2 ± 0.4	41 ± 4	10.827 ± 0.026	10.117 ± 0.046
ESO 501-G023	10:35:23.3	-24:45:15	0.76 ± 0.03	1.04 ± 0.14	0.134 ± 0.017	30.30	12.51	< 0.6	0.90 ± 0.09	9.9 ± 1.0	...	...
UGC 6446	11:26:40.4	+53:44:48	1.19 ± 0.02	0.44 ± 0.09	0.43 ± 0.06	21.00	21.00	< 0.4	0.97 ± 0.10	9.5 ± 1.0	...	...
NGC 3794	11:40:54.3	+56:12:07	2.37 ± 0.016	7.3 ± 0.9	0.49 ± 0.06	21.00	21.00	0.72 ± 0.15	3.5 ± 0.4	13.0 ± 1.3	11.871 ± 0.039	11.005 ± 0.072
NGC 3906	11:49:39.9	+48:25:32	2.25 ± 0.02	7.7 ± 0.9	0.25 ± 0.03	21.00	21.00	0.37 ± 0.12	2.8 ± 0.3	14.0 ± 1.4	11.788 ± 0.045	11.007 ± 0.067
UGC 6930	11:57:17.4	+49:16:58	0.76 ± 0.03	6.8 ± 0.8	0.25 ± 0.03	21.00	21.00	1.31 ± 0.19	2.6 ± 0.3	29 ± 3	11.752 ± 0.037	11.153 ± 0.068
NGC 4519	12:33:30.3	+08:39:18	3.0 ± 0.03	44 ± 5	0.99 ± 0.13	51.91	18.77	2.9 ± 0.3	6.9 ± 0.7	36 ± 4	10.499 ± 0.037	9.548 ± 0.059
NGC 4561	12:36:08.2	+19:19:22	4.55 ± 0.03	7.9 ± 1.0	1.02 ± 0.13	21.00	21.00	0.68 ± 0.12	4.1 ± 0.4	14.8 ± 1.5	11.480 ± 0.046	10.617 ± 0.074
NGC 4713	12:49:58.0	+05:18:41	5.35 ± 0.03	35 ± 4	0.69 ± 0.09	21.00	21.00	4.5 ± 0.2	7.1 ± 0.7	44 ± 4	10.367 ± 0.026	9.737 ± 0.053
NGC 4942	13:04:19.1	-07:38:58	3.55 ± 0.04	10.1 ± 1.1	0.49 ± 0.06	22.00	21.00	1.4 ± 0.2	3.4 ± 0.3	12.9 ± 1.3	11.617 ± 0.058	10.428 ± 0.092
NGC 5964	15:37:36.2	+05:58:27	2.11 ± 0.05	9.0 ± 1.0	0.30 ± 0.04	21.00	21.00	0.89 ± 0.17	3.4 ± 0.3	40 ± 4	12.384 ± 0.058	11.794 ± 0.113
NGC 6509	17:59:25.2	+06:17:11	4.62 ± 0.03	41 ± 5	0.50 ± 0.07	21.00	21.00	6.0 ± 0.2	10.6 ± 1.1	42 ± 4	10.284 ± 0.024	9.663 ± 0.043
IC 1291	18:33:52.5	+49:16:42	6.02 ± 0.02	9.3 ± 1.0	0.70 ± 0.09	21.00	21.00	0.37 ± 0.08	2.4 ± 0.2	10.2 ± 1.0	13.125 ± 0.052	12.689 ± 0.152

NOTE. — Column 1: Object name. Column 2 and 3: RA and DEC (J2000.0) of the pointing center of the IRAM 30m CO(1-0) observations. All measurements within a 21''-diameter circular aperture are centered on these coordinates. Column 4: H $\alpha$  flux within a 21''-diameter circular aperture, corrected for Galactic extinction and N II emission. We quote only measurement uncertainties here. Column 5: PAH flux density within a 21''-diameter circular aperture. Column 6: Average integrated H I line intensity within a 21''-diameter circular aperture, measured from image convolved to have beam major and minor axes given in Column 7 and 8. Column 7 and 8: Beam major and minor axes of image used for HI line intensity measurement. Column 9: Integrated CO(1-0) line intensity. Non-detections are quoted as 3 $\sigma$  upper limits. Column 10: 4.5 $\mu$ m flux density within a 21''-diameter circular aperture. Column 11: Total 4.5 $\mu$ m flux density. Column 12: Total  $J$ -band magnitude from 2MASS, corrected for Galactic extinction. Column 13: Total  $K_s$ -band magnitude from 2MASS, corrected for Galactic extinction.

TABLE 3  
H $\alpha$  OBSERVATIONS

Galaxy (1)	$t_{663nb15}$ (min) (2)	Run(s) (3)	$t_{693nb15}$ (min) (4)	Run(s) (5)
NGC0337	2400	3	2400	3
PGC3853	1800	4	1800	1
PGC6667	4500	1,3	4500	1,3
ESO544-G030	5400	1,3	5400	1,3
UGC1862	4500	1,3	5400	1,3
ESO418-G008	2700	1	2700	1
ESO555-G027	2700	1	2700	1
NGC2805	2400	3	2400	3
ESO501-G023	3600	1	3600	1
UGC6446	3900	2	4200	2
NGC3794	6000	1,3	6000	1,3
NGC3906	3200	1,2,3	3000	1,2
UGC6930	3600	2	3600	2
NGC4519	3600	2	3600	2
NGC4561	3600	1	3600	1
NGC4713	2400	1,2	2400	1,2
NGC4942	4500	1,2	3600	2
NGC5964	3600	2	3600	2
NGC6509	4800	2	3600	2
IC1291	3600	2	3600	2

NOTE. — Column 1: Object name. Column 2: Total exposure time in the 663nb15 filter. Column 3: Observing run code. Column 4: Total exposure time in the 693nb15 filter. Column 5: Observing run code. Observing run codes are: (1) Jan 2007; (2) May/June 2007; (3) Nov 2007; (4) Jan 2008.

TABLE 4  
DERIVED PROPERTIES

Source (1)	$R_{21''}$ (2)	$\log \Sigma_{\text{HI}}$ (3)	$\log \Sigma_{\text{H}_2}$ (4)	$\log \Sigma_{\text{SFR}}$ (5)	$\log \Sigma_*$ (6)	$\log M_*$ (7)	$12 + \log(O/H)$ (8)	$l_*$ (9)	$\kappa$ (10)	$Q_{\text{gas}}$ (11)	$Q_*$ (12)	$Q_{\text{gas+stars}}$ (13)	$\log P_{\text{h}}$ (14)
NGC 0337	2.11	1.33	1.18	-1.67	2.49	9.9	8.93	1.7	0.17	2.7	2.9	2.0	5.32
PGC 3853	1.16	0.78	0.67	-2.68	1.88	9.1	8.68	1.6	0.22	12	8	5	4.42
PGC 6667	2.51	1.09	0.42	-2.44	1.73	9.3	8.75	2.4	0.12	4.8	6	3.2	4.50
ESO 544-G030	1.42	1.02	< 0.09	-2.83	1.51	8.6	8.46	1.1	0.12	6.0	5	2.9	4.39
UGC 1862	2.27	0.62	0.29	-2.70	1.67	9.2	8.70	1.5	0.07	7	3.0	2.3	4.04
ESO 418-G008	2.40	0.84	< 0.34	-2.72	1.40	8.7	8.50	1.1	0.07	4.5	3	2.0	4.21
ESO 555-G027	2.47	0.78	...	-2.44	1.77	9.3	8.74	1.9	0.12	...	5	...	...
NGC 2805	2.85	0.74	0.92	-2.28	1.93	9.8	8.91	2.3	0.041	1.8	1.6	1.1	4.52
ESO 501-G023	0.71	0.40	< 0.32	-3.16	1.01	7.8	8.00	0.72	0.12	16	8	5	3.77
UGC 6446	1.83	0.73	< -0.008	-3.21	1.01	8.6	8.47	1.1	0.07	6.5	5	2.9	3.88
NGC 3794	1.96	0.75	0.27	-2.64	1.93	9.2	8.72	1.5	0.15	12	5	3.9	4.26
NGC 3906	1.86	0.69	0.20	-2.42	1.94	9.1	8.67	0.93	0.09	8	2.1	1.8	4.27
UGC 6930	1.73	0.66	0.72	-2.63	1.62	9.1	8.66	2.1	0.18	11	10	6	4.24
NGC 4519	2.00	0.82	0.99	-1.93	2.46	9.8	8.90	2.0	0.22	8	4	3.7	4.83
NGC 4561	1.25	1.23	0.40	-2.32	2.15	8.9	8.58	0.69	0.14	4.2	2.3	1.7	4.98
NGC 4713	1.52	0.99	1.15	-1.98	1.99	9.2	8.70	1.4	0.25	6.3	7	4.0	4.94
NGC 4942	2.90	0.88	0.69	-2.35	2.52	10.0	8.96	1.8	0.12	5.8	2.1	1.9	4.72
NGC 5964	2.52	0.71	0.53	-2.44	1.70	9.5	8.82	3.4	0.055	3.9	3	2.2	4.11
NGC 6509	2.87	0.89	1.31	-1.92	2.18	9.7	8.88	1.7	0.22	4.7	6	3.3	5.06
IC 1291	3.21	1.10	0.17	-2.19	1.35	8.9	8.60	2.1	0.18	8	13	5	4.37

NOTE. — Column 1: Object name. Column 2: Physical size of 21'' (kpc). All surface density measurements are within a 21''-diameter aperture. Column 3: HI mass surface density ( $M_{\odot} \text{pc}^{-2}$ ). The typical uncertainty is 0.06 dex. Column 4: H $_2$  mass surface density ( $M_{\odot} \text{pc}^{-2}$ ), computed with  $X_{\text{CO}} = 2.8 \times 10^{20} \text{cm}^{-2} (\text{K km s}^{-1})^{-1}$ . The typical uncertainty is 0.07 dex. Column 5: SFR surface density, computed assuming the Kroupa-type IMF from Calzetti et al. (2007) ( $M_{\odot} \text{yr}^{-1} \text{kpc}^{-2}$ ). We assume a typical uncertainty of 0.2 dex. Column 6: Stellar mass surface density ( $M_{\odot} \text{pc}^{-2}$ ). We assign a typical uncertainty of 0.2 dex. Column 7: Total stellar mass ( $M_{\odot}$ ). We assign typical uncertainty of 0.3 dex. Column 8: Oxygen abundance derived from the total stellar mass and the mass-metallicity relation of Tremonti et al. (2004). We derive a typical statistical uncertainty of 0.11 dex, but note that strong-line metallicity methods return  $12 + \log(O/H)$  values as disparate as 0.5 dex. Column 9: Stellar scale length (kpc). We estimate the uncertainty to be 20%. Column 10: Epicyclic frequency (km/s/pc), evaluated at 5.25''. We estimate the uncertainty to be 30%. Column 11: Gas stability parameter. The typical uncertainty is 30%. Column 12: Stellar stability parameter. The typical uncertainty is 60%. Column 13: Combined gas and stellar stability parameter. The typical uncertainty is 40%. Column 14: Mid-plane pressure ( $\text{K cm}^{-3}$ ). The typical uncertainty is 0.17 dex.